Synaptic composition, activity, mRNA translation and dynamics in combined single-synapse profiling using multimodal imaging

Reuven Falkovich[1], Sameer Aryal[2], Jasmine Wang[1], Morgan Sheng[2,3], Mark Bathe[1,4,5,†]

[1] Department of Biological Engineering, Massachusetts Institute of Technology, Cambridge, MA, USA
[2] Stanley Center for Psychiatric Research, Broad Institute of MIT and Harvard, Cambridge, MA, USA
[3] Department of Brain and Cognitive Sciences, Massachusetts Institute of Technology, Cambridge, MA, USA
[4] Broad Institute of MIT and Harvard, Cambridge, MA, USA
[5] Harvard Medical School Initiative for RNA Medicine, Harvard Medical School, Boston, MA, USA
[†] Corresponding author. Email: mark.bathe@mit.edu

Abstract

The function of neuronal circuits, and its perturbation by psychoactive molecules or disease-associated genetic variants, is governed by the interplay between synapse activity and synaptic protein localization and synthesis across a heterogeneous synapse population. Here, we combine in situ measurement of synaptic multiprotein compositions and activation states, synapse activity in calcium traces or glutamate spiking, and local translation of specific genes, across the same individual synapses. We demonstrate how this high-dimensional data enables identification of interdependencies in the multiprotein-activity network, and causal dissection of complex synaptic phenotypes in disease-relevant chemical and genetic NMDAR loss of function that translate *in vivo*. We show how this method generalizes to other subcellular systems by deriving mitochondrial protein networks, and, using support vector machines, its value in overcoming animal variability in phenotyping. Integrating multiple synapse information modalities enables deep structure-function characterization of synapse populations and their responses to genetic and chemical perturbations.

Introduction

Synapses shape neural circuits by integrating developmental, chemical, genetic, and activity cues and information into decisions of plasticity and metaplasticity that depend on circuit context. They achieve this via a complex interplay between dynamic levels of synaptic proteins including receptor subunits[1], scaffolding proteins[2,3] and enzymes, mediated in part by local in situ translation[4,5], in addition to signaling events such as phosphorylation[6,7], calcium fluxes[8] and synapse activity via voltage changes and neurotransmitter release. While individual synaptic components and their interactions with various aspects of synaptic function have been elucidated, how these highly interdependent processes work in concert to regulate synaptic structure-function requires simultaneous measurements of synaptic composition and activity across multiple measurement modalities spanning protein, mRNA, and synapse activity.

The synaptic molecular system is compartmentalized and locally regulated, motivating synapse-targeted methods for their investigation such as synaptosome preparations[6,9-11] or microdissection[11-14]. Combined with innovative labeling strategies these approaches can yield a wealth[11] of detailed information on synaptic molecular composition. However, they lack single-synapse resolution required to resolve heterogeneity in both synapse composition and function, even amongst synapses of the same class[15]. Thus, "synaptomic"[16] approaches that can map the distribution of individual synapses, such as fluorescence or electron microscopy, provide additional valuable single-synapse ultrastructural and contextual information, yet they are typically limited either in biochemical or activity information, or both. To bridge this gap, high-dimensional multimodal synaptomics, which can provide both molecular and activity information across individual synapses, would be highly enabling for neuroscience. In particular, synaptic protein-activity interactions play central roles in the etiology and treatment of neurodevelopmental and psychiatric disorders[17-26], as evidenced by the prevalence of synaptic proteins among disease-associated genes and psychiatric drug targets[25,26]. This novel form of multimodal single-synapse data could generate new hypotheses regarding local synaptic regulation and interprotein and protein-activity dependencies, which may be crucial for understanding, predicting, and manipulating how synaptic changes via pharmacological or genetic perturbations shape neuronal circuits and their dependent cognitive processes.

Towards this end, we previously developed PRISM—Probe-based Imaging for Sequential Multiplexing to map synaptic protein levels in situ[27-29]. PRISM uses rapid and gentle salt-based exchange of fluorescent oligonucleotide probes on barcoded antibodies for quantitative immunofluorescence imaging of multiple proteins in the same neuronal culture, in a manner compatible with high-throughput superresolution multiplexing[27,30]. Automated analysis yielded distributions of millions of synapses in high-dimensional protein space[27,29,31], showing composition-defined subtypes of glutamatergic synapses, as well as complex synaptome-level phenotypes of activity perturbation[29] or RNAi of genes associated with schizophrenia and autism spectrum disorder[31]. Bayesian network inference yielded network models of protein dependencies that predicted causal protein-protein effects inaccessible to conventional IF. However, neuronal circuits are shaped by the myriad processes connecting synaptic transmission and protein composition, and measuring synaptic activity and

proteins simultaneously is necessary to discern how these processes operate in concert and across the synapse population, and to directly observe function-composition dependencies which were hitherto only inferred indirectly, such as between active or silent synapses defined pre- and postsynaptically[32,33]. In addition, local regulation of synaptic protein translation is known to play a central role in normal as well as disease-associated or aberrant synaptic function[12,34], for example in the case of fMRP[35,36]. Thus, measuring local translation processes alongside activity and multiprotein composition in individual synapse is necessary for a more comprehensive picture of synaptic processes.

To achieve this, here we combined PRISM and Bayesian network analysis with *in situ*, single-synapse-resolution imaging-based sensors for calcium content[37], glutamate release[38], and gene-specific translation[39], to perform simultaneous measurements of multiprotein content, calcium/glutamate spiking, and multi-gene translation activity across millions of individual synapses in neuronal culture. This united approach, which we term Multimodal-PRISM, reveals protein correlates of synaptic activities, identifies network mediators of treatment effects and correlations between proteins and activity parameters, and recovers dynamic signaling pathways from kinetic pulse-chase experiments. Importantly, it also generalizes beyond the synapse, recovering expected local interdependencies amongst mitochondrial proteins and identifying a tentative new process in synaptic mitochondria.

We applied Multimodal PRISM to study synaptic regulation of NMDAR subunit levels, having previously observed potentiation in synaptic protein levels in Grin2a siRNA-mediated knockdown[31] and similar responses to chronic NMDAR antagonism. We discovered that both genetic and pharmacologic reductions of global NR2A production elicit a compensatory response that involves increased local synaptic translation of scaffolding proteins such as CaMKIIa and increased potentiation evidenced by calcium trace shapes, glutamate spiking activity and protein localizations. These relationships are (1) manifested locally; (2) reversed in NR2A-specific antagonism; (3) predicted by the structure of the multimodal Bayesian network; and (4) interdependent in a manner that can be inferred from the network structure. Finally, we demonstrated the value of multimodal distribution phenotyping in overcoming individual variability using support vector machine[40] (SVM) classifiers,.

Results

Live imaging of synaptic activity integrated with multiprotein measurement

To elucidate causal dependencies between synapse protein composition and synaptic activity, we first sought to combine single-synapse activity trajectories with PRISM multiprotein imaging of the same synapses post-fixation. In our first reported method, termed Calcium Timelapse PRISM (“CAT-PRISM”), we targeted calcium ion concentration dynamics which can be imaged using organic indicators. Since we anticipated slowly changing post-synaptic calcium levels to dominate the signal[41-45], we imaged, in DIV 14 cultures, 30–60 minute-long timelapses at 3–6min per frame (Methods) to extract individual postsynaptic calcium traces over time. To enable assignment of synaptic calcium puncta to post-fixation synaptic PRISM signals, we used Hoechst staining

present during both live and PRISM imaging, to align pre- to post-fixation images with a precision of ~3–4 pixels, corresponding to ~2–3 microns (Methods, Fig. S1a).

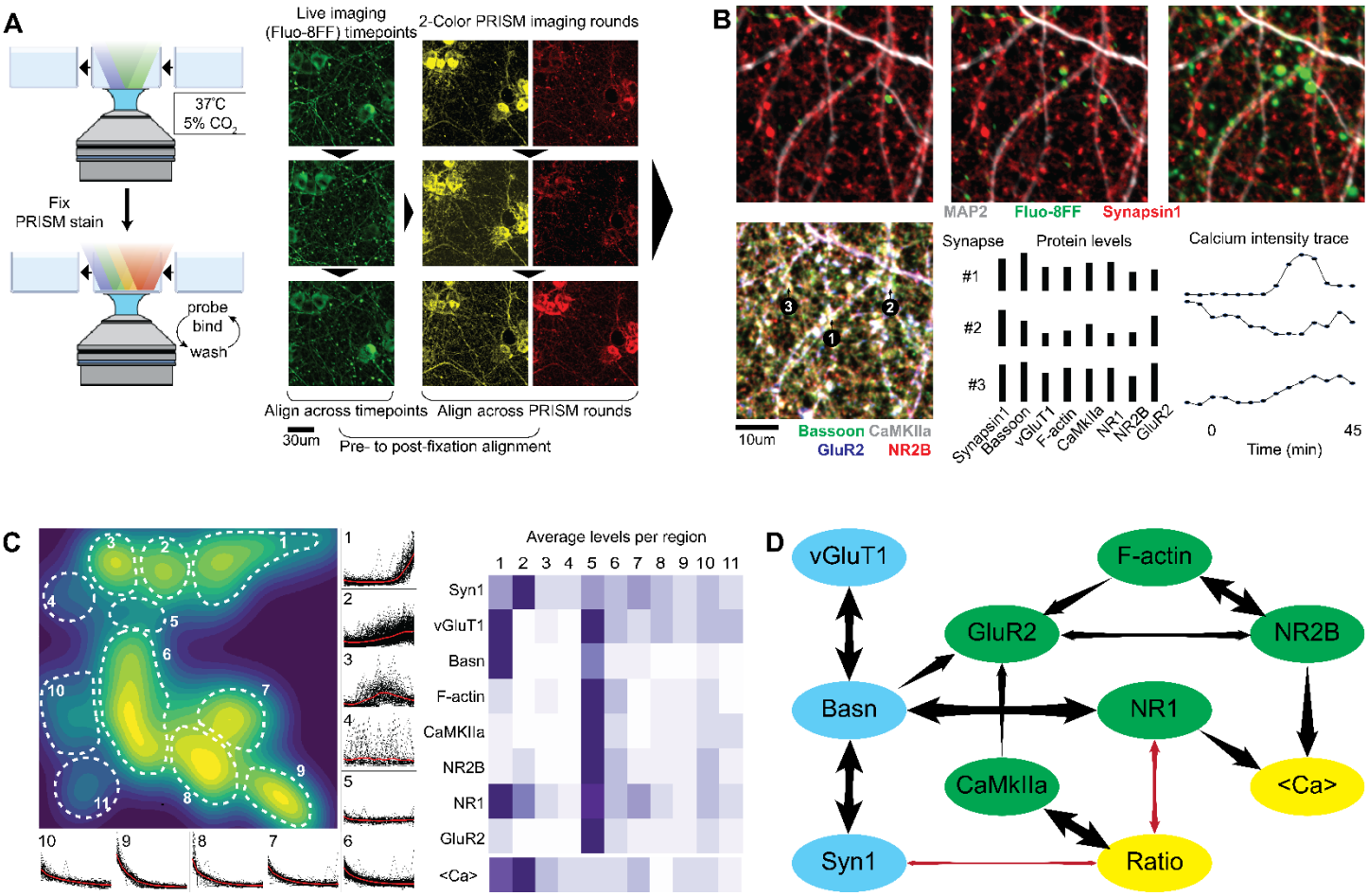

Figure 1: Calcium-PRISM imaging. A) Schematic of tandem live-PRISM imaging. Alignment is performed via Hoechst stain present in both live and fixed images (Fig. S1a). B) Resulting images from the same FOV across rounds. Top row: Three timepoints of pre-fixation calcium images (green) overlaid with post-fixation Synapsin1 (red) and MAP2 (white). Bottom left: Four synaptic proteins from different PRISM imaging rounds. Bottom right: Measured relative protein levels and calcium traces for individual identified synapses. C) The distribution of synapses in combined high dimensional space of protein levels and calcium trace shapes. Left: Density contours of UMAP projection with manually delineated regions. Middle: Mean-normalized calcium trace shapes and average trace (red) in each region. Right: Average levels of synaptic proteins and calcium in each region. D) Bayesian network connecting measured variables. Arrow widths correspond to edge strengths. Blue – presynaptic proteins, Green – postsynaptic proteins, Yellow – activity parameters.

In combined calcium-PRISM imaging at DIV 14 (Fig. 1a and b, Supp. Video 1), we identified that 35% of Synapsin1 puncta had corresponding calcium puncta from live-imaging. In order to visualize the distribution of calcium trace shapes, we performed dynamic time warping (DTW)[46] (Methods) on mean-normalized traces, which groups traces of similar shapes closer together. The resulting distribution of calcium trace shapes was mostly one-dimensional (Fig. S1b-c) with most traces monotonously increasing, decreasing or constant, and with additional differences corresponding to the abruptness of signal change and a small fraction of calcium-spiking puncta. Average synaptic calcium levels were consistently lower under APV NMDAR inhibition, whereas under TTX activity blockade they were initially higher than untreated synapses but subsequently lower over time (Fig. S1d).

We combined DTW-analyzed calcium trace information with PRISM measurements of eight proteins—Synapsin1, Bassoon, vGluT1, F-actin, CaMKIIa, GluR2, NR1, NR2B—in the same synapses (Methods) to yield a high-dimensional composition-activity distribution (Fig. 1c) with clusters defined both by presence or absence of synaptic proteins and by calcium levels and trace shapes (Fig. 1c). In order to analyze this distribution in depth and identify direct protein correlates of synaptic activity that are not mediated by other proteins, we extracted two main parameters describing calcium fluxes. The first was mean calcium level over time ("<Ca>") and the second was the ratio of calcium level at the one-hour timepoint relative to the level at time zero ("Ratio"). Bayesian network analysis on the combined distribution of these two parameters and eight protein levels identified NMDAR subunit levels (NR1 and NR2B) as directly correlated to average calcium levels (Fig. 1d), as anticipated. Calcium level increase, on the other hand, was directly correlated to levels of CaMKIIa and negatively correlated with NR1 when controlling for all other proteins.

In our second reported method, termed Glutamate Release Loci PRISM ("GRL-PRISM"), we sought to incorporate a more direct indicator of synaptic activity by imaging single-synapse glutamate release events ("spikes") using iGluSnFR3, a recently developed glutamate sensor with kinetics and signal-to-noise suitable for single synapse detection of minis and transmission events[38]. DIV 14 neurons transduced with iGluSnFR3 were imaged at 10–20ms exposures, collecting 50–100 consecutive snapshots over 1–2s windows (Supp. Video 2) (Methods). Live images were aligned to post-fixation PRISM images as described above. Spiking puncta were automatically identified using pixel-by-pixel spike detection on spatially smoothed images (methods, Fig. S1F) and assigned to post-fixation Synapsin1 puncta (Fig. 2a) to enable combined analysis of ten protein measurements—the above set plus PSD95 and phospho-CaMKIIa—with spiking behavior of single synapses. Only a subset of Synapsin1 puncta are glutamatergic synapses, only a subset of these will be active, and only a subset of active synapses will be observed as firing during the short recording window employed. Thus, only 10% of Synapsin1 puncta had overlapping glutamate spiking puncta although that number climbs to 20% when considering only synapses positive for all excitatory markers.

Both the frequency and intensity of Synapsin1-associated optical spikes increased over time in chemical LTP-induced cultures (20uM Bicuculline + 200uM glycine) over Bicuculline control (Fig. 2b), whereas under TTX activity blockade optical spike frequency was reduced but not to zero, as observed by others[38], presumably due to mini events. Mapping the distribution of synapses in 10-dimensional protein space (Fig. 1C) revealed that synapses with at least one glutamate spike were drawn from a markedly different synaptic protein distribution than non-spiking ones. Specifically, they were enriched in regions 1 (all proteins present at high levels) and 2 (all proteins present at lower levels and GluR2 higher) at the expense of other regions, which lacked GluR2 and other protein combinations (Fig. 1D).

We then sought to perform a more systematic analysis of the protein correlates of glutamate spiking, and specifically of three aspects of activity: (i) existence of a spike, (ii) overall intensity of spikes, and (iii) increase in spike intensity, which indicates synaptic potentiation. We performed a logistic regression for measure (i) and

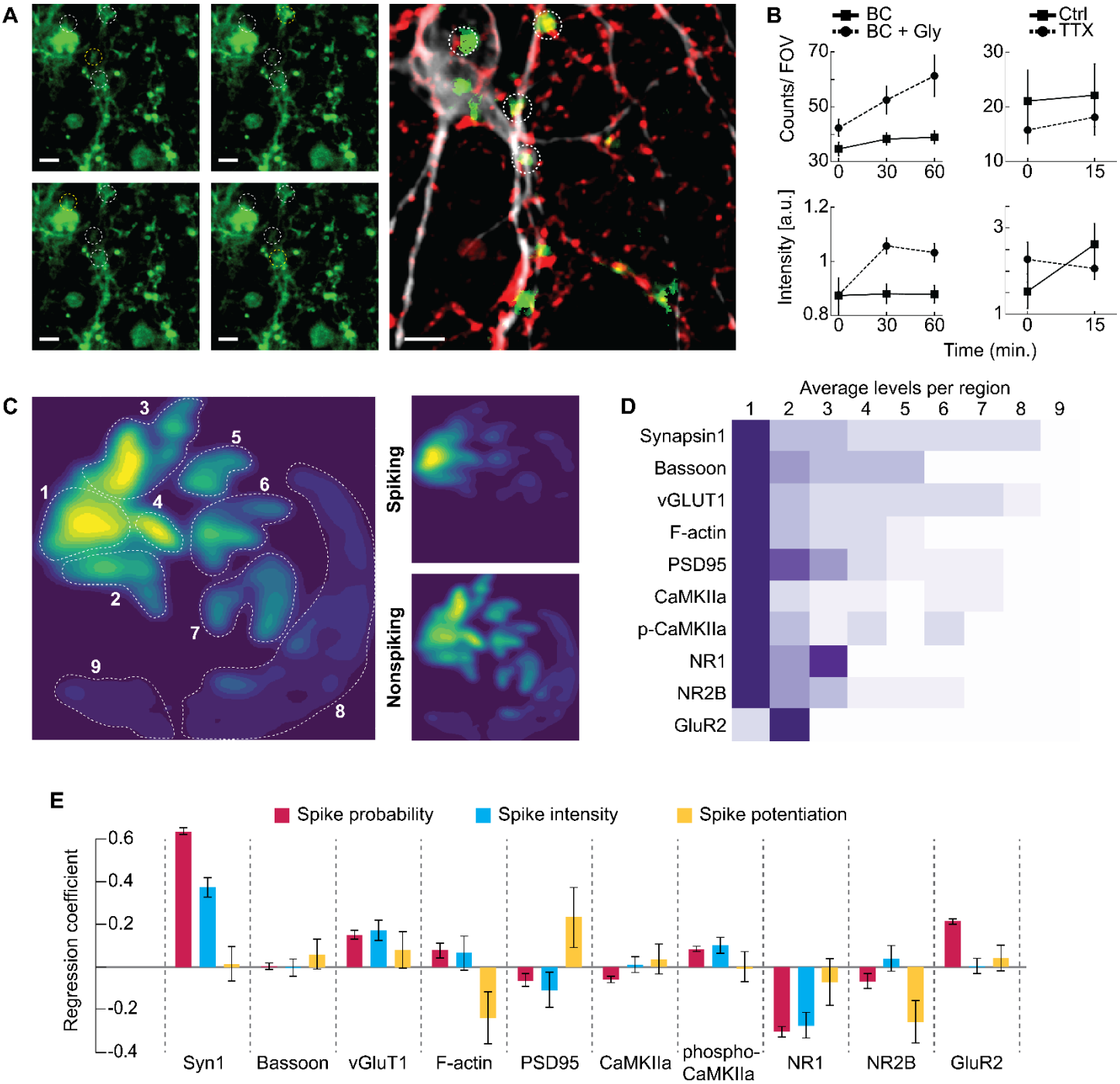

Figure 2: Glutamate-PRISM. A) Left: Four frames of the same FOV, each with a different region spiking relative to the other three regions (circled). Right: The same FOV, overlaying spike detection output (green) with post-fixation Synapsin1 staining (red) and MAP2 (white). Scale bar is 10um B) Spike counts and average intensity at different times during treatment with chemical LTP (Left, Bicuculline + glycine, compared to Bicuculline baseline) and TTX (Right) Error bars are mean ± s.e.m across wells. C) Distribution of synapses in protein space (density contour plot of UMAP projection). Small: sub-distributions of synapses with and without a detected spike. D) Relative average protein levels of regions delineated in (C). E) Regression coefficients of spiking paramaters against the nine measured proteins. Red: logistic regression for spiking binary outcome. Blue: Linear regression for spike intensity among spiking synapses. Yellow: Difference between spike intensity at 1 hour and at start. Error bars are S.E. of the regression.

linear regressions for measures (ii) and (iii) against the ten measured proteins (figure 1E). We observed that Synapsin1 and vGluT1 were strong predictors of spiking probability and intensity, as expected of vesicular proteins. The coefficients of Synapsin1 are partially artifactual since Synapsin1 puncta were used to define synaptic regions in images and protein overlap with them was used to assign spiking analysis puncta to synapses, which was more likely when puncta were larger.

Phosphorylation of CaMKIIa was also predictive of spiking probability and intensity, consistent with its dependence on calcium influx from synapse activity and its contribution to LTP. We were surprised to observe strong negative coefficients of NR1 in spiking probability and intensity. When simultaneously measuring NR1 (which accounts for both NR2A and NR2B-containing NMDARs) and NR2B, the remaining variance in NR1 was at least in part due to NR2A levels. This indicates a negative dependence of synapse glutamate activity on NR2A with constant NR2B and GluR2, which we explored further in section 4. Regression coefficients of spiking potentiation indicated negative and positive coefficients for F-actin and PSD95, respectively, as well as a negative coefficient for NR2B (Fig. 2e). A hypothetical interpretation of this observation is that larger dendritic spines with smaller amounts of scaffolding and receptor proteins indicates a synapse in the process of being reduced or eliminated prior to the spine shrinking as well, whereas larger amounts of PSD95 with smaller dendritic spines may indicate a synapse in the process of potentiating[47].

Finally, GluR2 had the second-highest coefficient for spiking probability but no contribution to spike intensity, reinforcing our observation of binary categories of silent and active synapses. Combined with the observation of GluR2-containing synapse clusters enriched among spiking synapses, this suggests a correspondence between presynaptically silent and active synapses (defined by vesicle release)[32] and postsynaptically silent and active synapses (defined by AMPAR presence)[33] and reinforces the importance of combining activity and protein measurements of the same synapses.

Integration of *in situ* mRNA translation into Multimodal-PRISM

In order to incorporate *in situ* measurement of gene-specific local synaptic translation into PRISM, we developed RIBOmap-PRISM (Methods), an adaptation of ribosome-bound mRNA mapping (RIBOmap)[39] to PRISM probe-exchange multiplexing. RIBOmap identifies putative mRNA translation events *in situ* using coincidence detection between mRNA transcript-specific primer and padlock probe pairs and a probe against the 18S ribosomal RNA. The combination of all three generates a single-stranded RCA amplicon when spatially co-localized. In RIBOmap-PRISM, the resulting amplicon presents a docking strand, which can then be imaged in a standard PRISM protocol alongside PRISM barcoded antibodies (Fig. 3a).

We observed puncta of translation events of *Actb* (β-actin), *Dlg4* (PSD95), *Camk2a* (CaMKIIα) and *Ntrk2* (TrkB) (Fig. 3b). Identifying synapses, dendrites and soma with Synapsin1 and MAP2 staining in the same sample (Methods) allowed us to assign RIBOmap-PRISM puncta to these neuronal regions (Fig. 3c) and compare with other measurements of subcellular transcript localization and translation, specifically somatic versus neuropil ribosomal profiling (Ribo-Seq) from microdissected tissue[12]. Counting puncta enrichment in dendrites versus

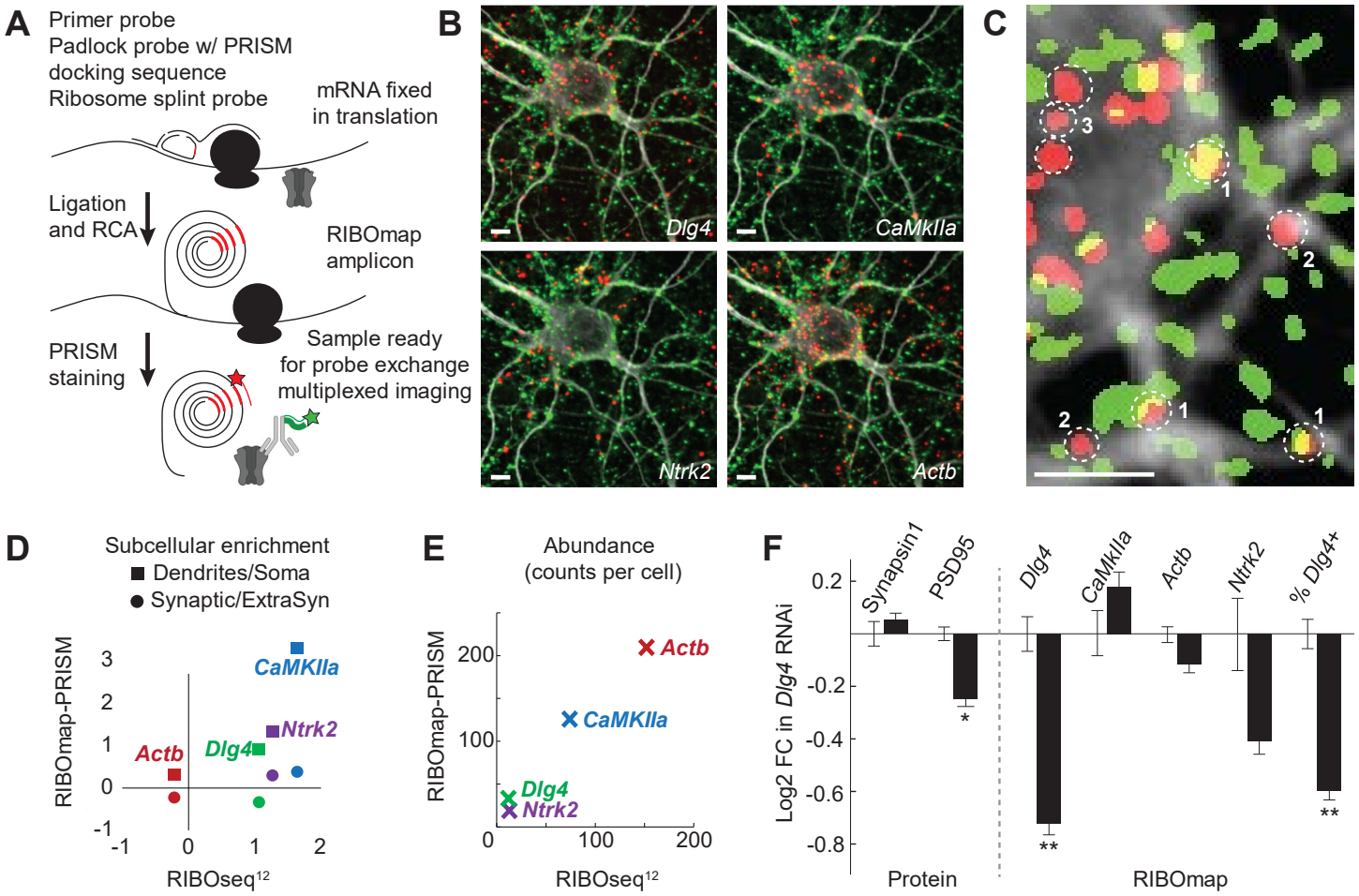

Figure 3: RIBOmap-PRISM. A) Generating PRISM readout of proteins and currently translating mRNA in the same sample using PRISM-adapted RIBOmap. B) RIBOmap-PRISM images (red) of four genes in the same sample, overlaid with Synapsin1 (green) and MAP2 (white), from combination of different imaging rounds. C) RM-Dlg4 (red) and Synapsin1 (green) segmented puncta, overlaid with MAP2 (white). Three types of RIBOmap puncta are identified: synaptic (1), dendritic extrasynaptic (2), somatic extrasynaptic (3). D) Y-axis; squares: Dendrite versus soma localization of puncta of different genes (log2 ratio of puncta counts). Circles: synaptic vs extrasynaptic localization. X-axis; Neuropil versus soma enrichment from Glock et al. E) Estimates of puncta count per cell count (Methods). Y-axis; this study. X-axis; Glock et al. F) Effect of Dlg4 RNAi on average synaptic levels of protein and RIBOmap signals and on % of synapses which contain a Dlg4 RIBOmap puncta. Scale bars are 20uM. *p<0.05, **p<0.01

soma, we observed that the four genes measured follow the same pattern as neuropil/soma enrichment levels measured by Ribo-Seq (Fig. 3D, squares), despite the difference in model systems and measurement approach. Measuring synaptic vs non-synaptic enrichment using colocalization with Synapsin1 (Fig. 3d, circles) showed *Camk2a* and *Ntrk2* translation as preferentially localized to synapses specifically and not just neuropils. Estimates (Methods) of the number of identified translation events per cell in RIBOmap-PRISM matched those from Ribo-Seq (Fig. 3e). Both synaptic PSD95 protein and *Dlg4* RIBOmap-PRISM signals were reduced (20% and 40%, respectively) with siRNA-mediated knockdown of *Dlg4* (Fig. 3f).

To test whether amplicons generated by RIBOmap-PRISM crowd each other or affect accessibility of protein antigens in tight synapses, we looked at Synapsin1 signal and probability of *Ntrk2* puncta colocalization in synapses containing *Dlg4* RIBOmap-PRISM puncta that underwent different amplification times. Neither were affected despite a 7-fold increase in RCA amplicon size as indicated by *Dlg4* RIBOmap-PRISM fluorescence integral (Fig. S2a). We also observed (Fig. S2c) that even at low amplification times puncta intensity distribution was approximately exponential with a single mode, consistent with the expected distribution of single amplicon sizes[48], indicating a negligible population of two or more sources. This is consistent with observations of few polysomes and ~2–3 translation events per synapse[49] at the moment of fixation. Thus, for all subsequent analyses, we treated the RIBOmap-PRISM signal as a binary variable indicating presence of a single ribosome-associated mRNA for a specific gene.

PRISM network inference recovers dynamic TrkB-BDNF signaling pathways and mitochondrial protein level interdependencies

We sought to test our multimodal imaging and network analysis approach in two scenarios beyond steady-state synaptic protein levels. First, in analyzing dynamic signaling networks manifesting in synaptic protein phosphorylation states, and second, in analyzing protein inter-dependency networks in mitochondria.

For dynamic network inference, we examined one branch of the BDNF response pathway that is largely compartmentalized to the synapse[50-52]: TrkB → Akt → mTORC1 → P70S6K → S6RP → activated translation. To test synaptic response along this branch, we performed PRISM measurements using phospho-specific antibodies against p-TrkB, p-Akt, p-S6KP70 and p-S6RP, as well as four other synaptic targets including NR2A, at different time points after stimulation with BDNF, and in the presence or absence of the mTOR inhibitor rapamycin.

Levels of individual phosphorylated proteins followed expected kinetics[50] in the order in which they were activated (Fig. 4A). Rapamycin abolished the increased phosphorylation of P70S6K and S6RP, both downstream of mTORC1. Interestingly, NR2A levels increased cumulatively up to 75% with BDNF treatment, an increase that

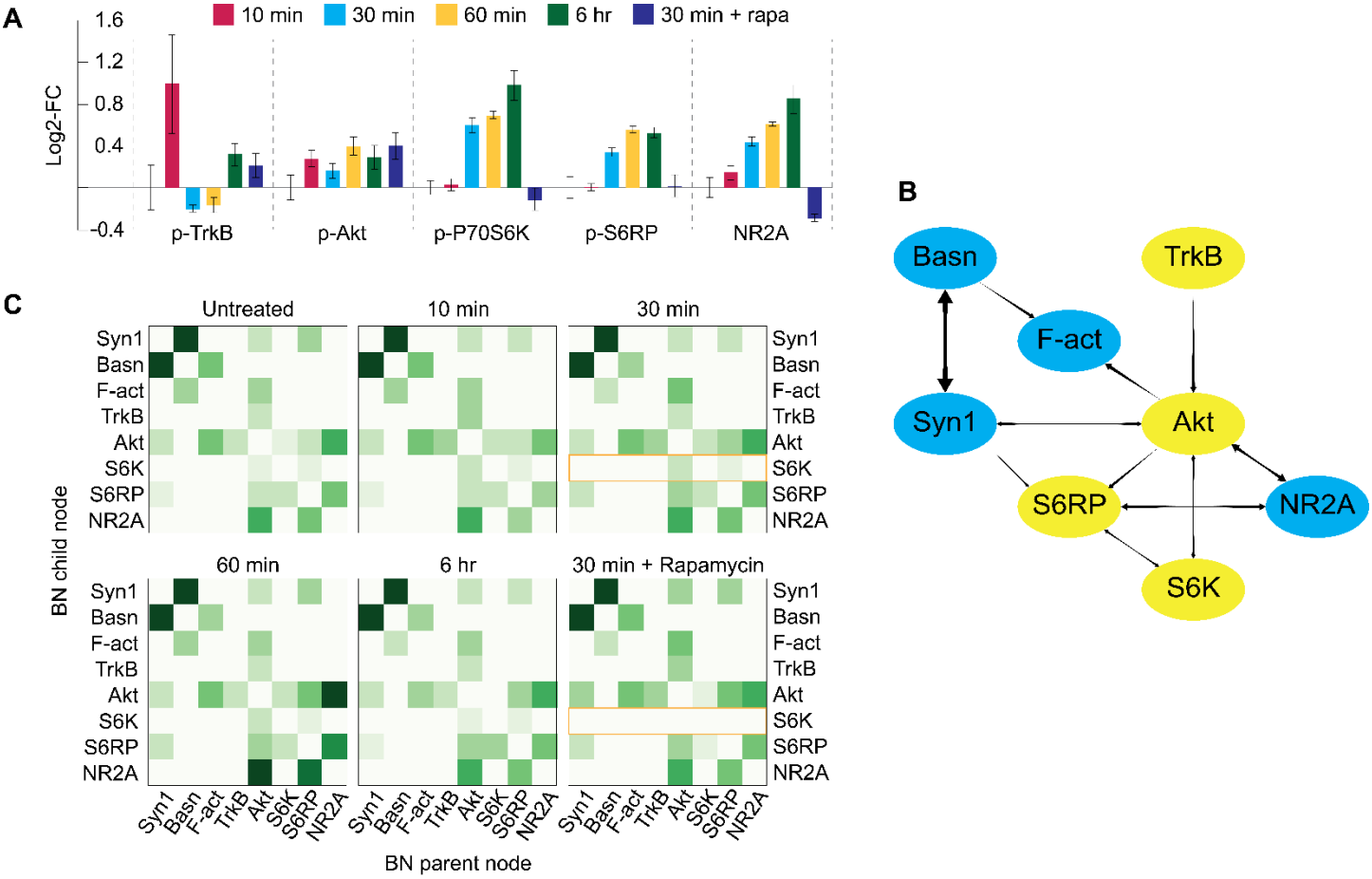

Figure 4: Bayesian network inference on a dynamic phosphorylation cascade. A) Log_2 fold change in average synaptic levels of phosphoproteins and NR2A at different time points after BDNF treatment. Bars are mean±s.e.m. B) Combined Bayesian network inferred from individual distributions. See alternative thresholding in Fig. S4. C) Relative network edge strengths in each treatment group.

was also abolished by rapamycin, indicating a dependence of NR2A on local synaptic translation regulation, even though its gene, *Grin2a*, is not locally translated[12].

We then used static Bayesian network inference on the distribution from untreated cultures, generating the network in Fig. 4B. This network exhibited the anticipated Synapsin1-Bassoon-F-actin interdependency, and partially retrodicted the signaling pathway with TrkB upstream of Akt and S6K, S6 and NR2A downstream of it. Using this model, we tested changes to network edge strengths at different time points after BDNF treatments (Fig. 4C). We observed the non-pathway protein edges (Synapsin1, Bassoon, F-actin) remaining relatively constant while the edges between pathway proteins changed strengths over time. Finally, when comparing the network edge strengths at 30min following BDNF treatment with and without rapamycin, the only noticeable difference we observed was the weakening of all edges leading to p-P70S6K (Fig. 4C, highlighted yellow). This demonstrates the ability of MINI-ME based phenotyping of network edges to identify perturbations to proteins that are not measured directly, in this case, mTORC1, which is directly upstream of P70S6K[53].

To evaluate PRISM in a distinct molecular system from the neuronal synapse, we chose the mitochondrial protein network as a similarly small, highly compartmentalized and locally regulated[54-56] system, with tight protein homeostasis maintained by gene expression from a local genome[57] and by intricate protein import, quality control, chaperone, and degradation machineries within and across the inner and outer membranes[58]. Mitochondria are also plastic, performing molecular computation to guide stem cell decision making[59], and neuronal mitochondria are affected in psychiatric[60,61] and neurological[60] disorders with synaptic mitochondria crucial for activity and vesicle regeneration[62]. We chose eight mitochondrial proteins to examine: Three translocase machinery components (outer membrane translocase subunits Tom20 and Tom40, and inner membrane translocase subunit Tim23); four OxPhos pathway components (C4 subunits Cox2 and Cox4, C1 protein NDUFA9 and C3 protein UQCRC2); and finally ATPI1F, an inhibitor of ATP synthase (C5). We imaged these eight proteins in DIV 14 rat hippocampal neurons alongside MAP2, Synapsin1, and GluR2 for subcellular assignment of mitochondria.

Mitochondrial proteins showed punctate staining along dendrites (Fig. 5A), similar to previous observations. Puncta of each protein were automatically segmented by CellProfiler (Fig. 5A, bottom left), and high-confidence mitochondrial puncta, defined as those positive for at least three mitochondrial proteins, were used for subsequent analysis. Since individual mitochondria were less well-defined than synapses, and segmentation of these reticulate structures into small puncta somewhat random, we used local protein concentration per “mitochondrial region”—measured using the average signal of each protein—for individual data points rather than total protein level measured with the integrated signal employed for synapses.

The Bayesian network of mitochondrial proteins (Fig. 5b) bore out the prediction that proteins belonging to the same pathway (oxphos or protein import) would be more tightly dependent on each other than across pathways, presumably due to the need for stoichiometric control and colocalization of proteins facilitating different stages

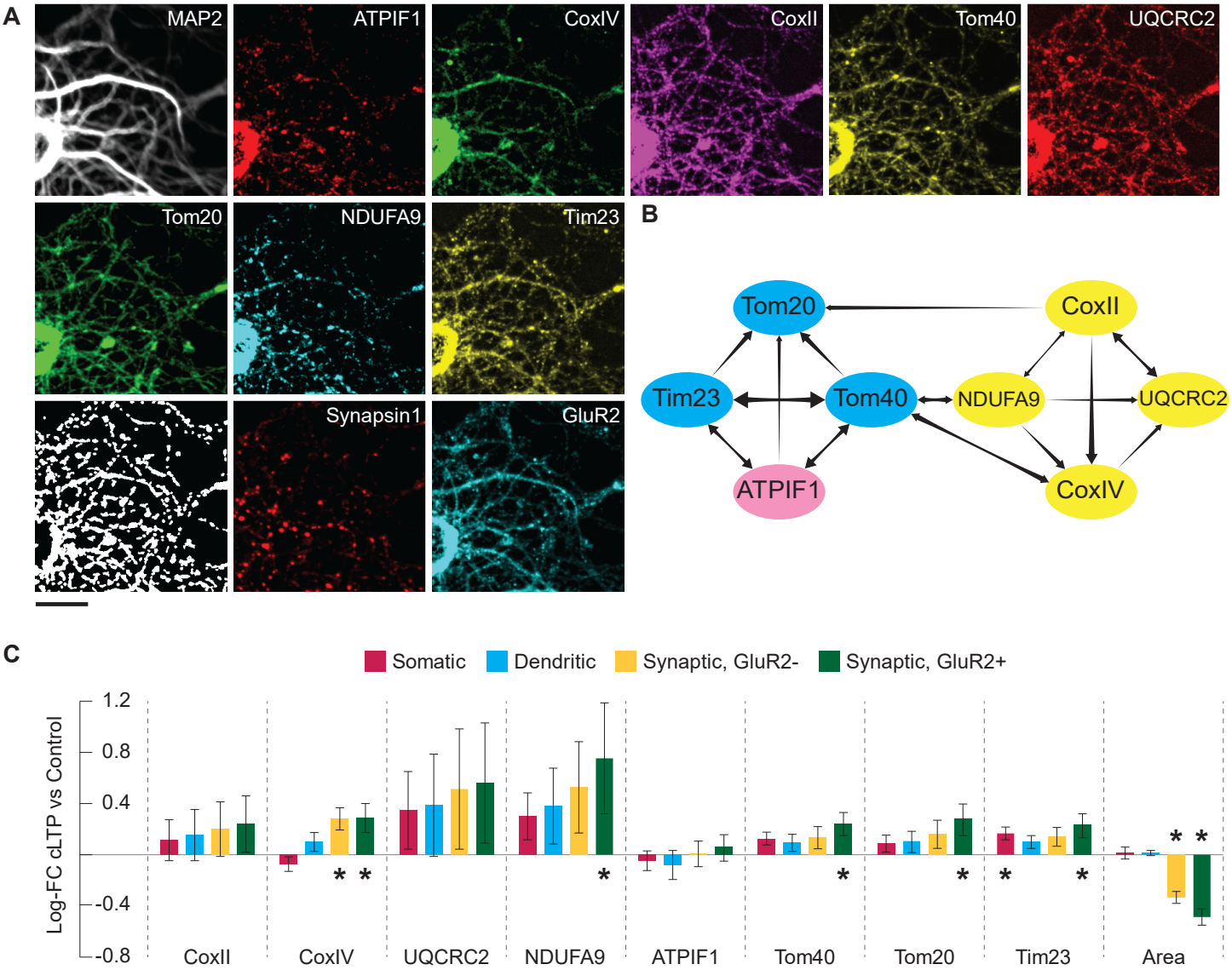

Figure 5: Mitochondrial PRISM network inference. A) Images of the same neuronal culture across PRISM rounds. Left to right, top to bottom: MAP2, ATPIF1, CoxIV, CoxII, Tom40, UQCRC2, Tom20, NDUFA9, Tim23. Bottom row, left to right: automatically segmented mitochondrial puncta, Synapsin1, GluR2. Scale bar is 50um. Somatic mitochondrial staining is oversaturated to make dendritic/synaptic mitochondria more visible. B) Bayesian network of eight mitochondrial proteins, color coded by pathway. C) Log_2 fold change of each protein and total area of neuronal mitochondria of four types, in cLTP-treated versus untreated cultures. Error bars are mean±s.e.m. *p<0.05.

of the same process[63]. We were also interested in the causal dependency of ATPIF1 levels, an inhibitor of ATP synthase, since on the one hand it interacts with the OxPhos complex, but it is not an integral part of it and not necessarily stoichiometrically constrained. On the other hand, ATPI1F is imported by the translocation machinery and thus possibly limited by its presence. Bayesian network analysis suggested that the latter plays a stronger role in determining local mitochondrial ATPI1F levels. We repeated these measurements in HeLa cells, deriving a similar Bayesian network of local protein concentrations despite the mitochondria appearing morphologically distinct (Fig. S3a–b).

Finally, we were interested in mitochondrial response to synaptic chemical perturbation. 75% of mitochondria were associated with neurons. Using the MAP2, Synapsin1 and GluR2 stains we assigned these mitochondria (Fig. S3c) either to soma (~17% of mitochondria), extra-synaptic dendritic regions (~45%), and to synapses

(11%), associated with either GluR2 positive/active (2.5%) or negative/silent (8.5%). Treatment with chemical LTP for 30min prior to fixation led to an increase in mitochondrial OxPhos machinery that is specific to synaptic mitochondria and was stronger in mitochondria associated with active synapses, alongside an overall decrease in the total area of synaptic mitochondria (Fig. 5C). This paints an overall picture of synapse-associated mitochondria contracting to increase local density of OxPhos machinery in response to cLTP.

Combined Activity-Translation-Multiprotein Bayesian network predicts complex synaptic responses to NR2A depletion and chemical inhibition which extend to genetic Grin2a models

We combined the modalities described above to perform tandem imaging of calcium, mRNA translation of three synaptic genes, and eight synaptic proteins, in the same neuronal cultures (Fig. 6a) (Multimodal-PRISM). We constructed a Bayesian network unifying the eight protein measurements, four translation measurements (overall puromycin incorporation, *Dlg4*, *Camk2a* and *Ntrk2*), and two activity measurements consisting of calcium signal at the outset and ratio of final-to-initial calcium (Fig. 6b, presented as a heatmap of edge strengths due to the large number of nodes). We observed typical edges connecting Bassoon to Synapsin1 on the presynaptic side and to F-actin, PSD95 and CaMKIIa on the postsynaptic side, as well as edges connecting PSD95 to GluR2 and NR2A. RIBOmap signals were not strongly correlated with their corresponding proteins, which was expected given that the former was a snapshot of translation activity at the moment of fixation and the latter was a cumulative, steady-state level. They were however correlated with overall translation activity reported by puromycin. Many postsynaptic proteins, including NR2A, which we already observed to be responsive to BDNF-induced potentiation and sensitive to mTORC1 inhibition, exhibited strong dependencies on overall synaptic and specifically *Ntrk2* translation, possibly as an indirect reporter of TrkB activation and turnover[64].

We observed that average calcium levels were directly correlated with NR2A and GluR2 abundance and active zone size, whereas calcium increase was directly correlated with CaMkIIa, similar to observations in figure 1. Surprisingly, however, strong negative edges were found between NR2A and CaMKIIa/GluR2. This predicts that, unless edges change by perturbing an unmeasured node, lower NR2A can lead to an increase in CaMKIIa and GluR2, a decrease in average synaptic calcium, and an increase in the ratio of calcium increase. These suggest a mechanism by which reduced *Grin2a* expression leads to increased excitatory synaptic proteins and synapse density, as we observed previously[31].

To test this relationship predicted by the Bayesian network, as well as by the network and regression coefficients in figures 1e and 2e, respectively, and to study this mechanism in more detail, we used chronic NMDAR blockade with APV, which we previously showed partially recreates the *Grin2a* knockdown phenotype[31], and performed multiplexed protein, translation and activity measurements on DIV 7, 10 and 14 cultures treated from DIV 5 with APV and fixed one hour after removing APV (Fig. 6c-g). Chronic APV treatment at from DIV 5-10 led to lower starting synaptic calcium but a higher increase in calcium over an hour after drug removal compared with untreated cultures (Fig. 6c). This stronger potentiation was exacerbated in synapses with higher starting calcium level (Fig. S4a), showing that this was not a saturation effect. It also manifested in glutamate spiking, with a 5-fold higher increase in number of glutamate spikes after an hour, relative to untreated cultures. Looking at changes to synaptic protein translation and levels at DIV 7-14 cultures (Fig. 6e), we observed strong accumulating or sustained increases in local translation especially of CaMKIIα (3-fold), with corresponding 4-fold increases in synaptic CaMKIIα and increases in all other proteins except NR2A (Fig. 6d), which was transiently lower at

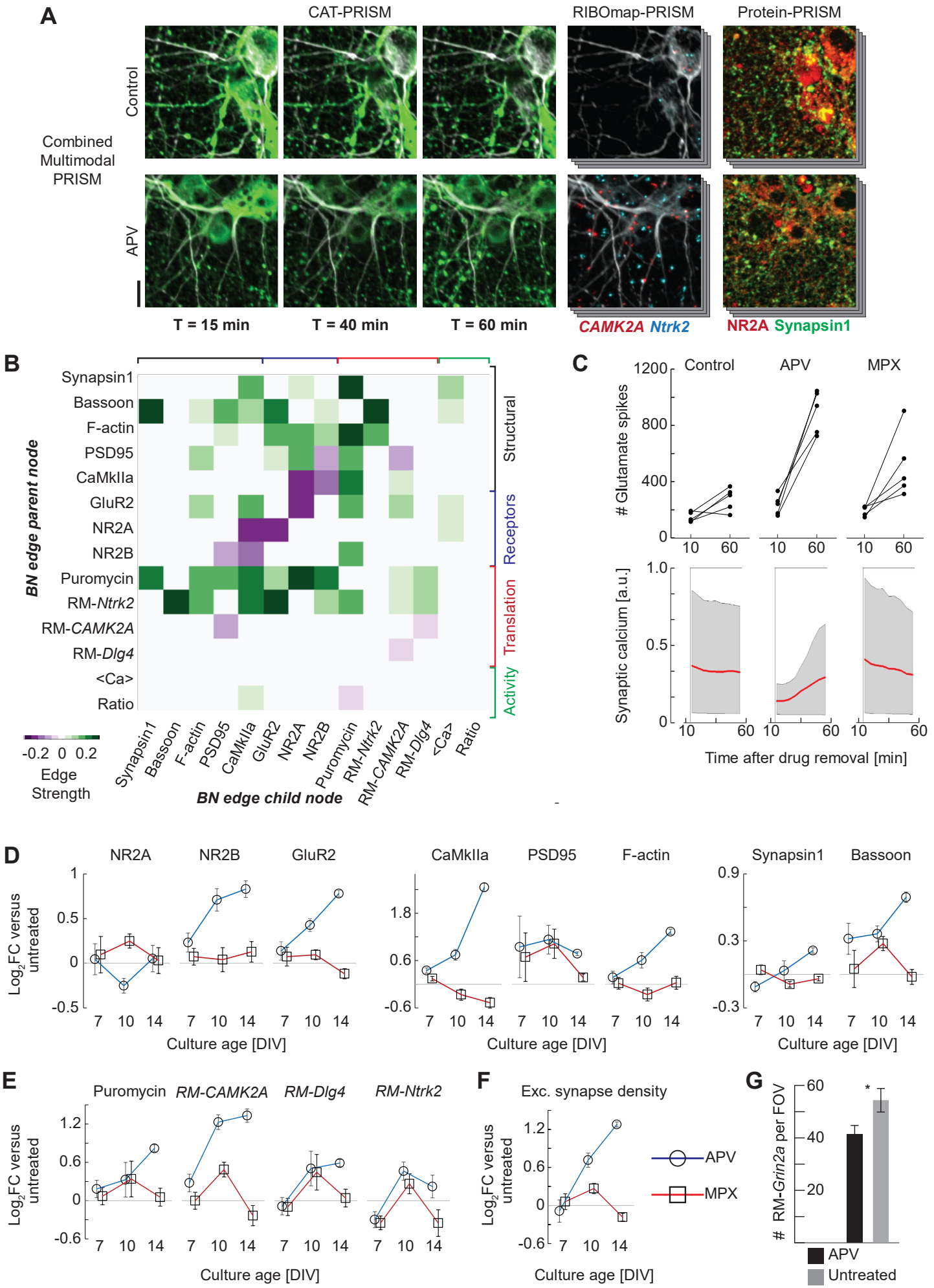
A
CAT-PRISM
RIBOmap-PRISM
Protein-PRISM
Control
APV
Combined Multimodal PRISM
T = 15 min
T = 40 min
T = 60 min
CAMK2A Ntrk2
NR2A Synapsin1
B
BN edge parent node
BN edge child node
Synapsin1
Bassoon
F-actin
PSD95
CaMkIIa
GluR2
NR2A
NR2B
Puromycin
RM-Ntrk2
RM-CAMK2A
RM-Dlg4
<Ca>
Ratio
Structural
Receptors
Translation
Activity
-0.2 0 0.2
Edge Strength
C
Control
APV
MPX
Glutamate spikes
Synaptic calcium [a.u.]
Time after drug removal [min]
D
NR2A
NR2B
GluR2
CaMkIIa
PSD95
F-actin
Synapsin1
Bassoon
Log2FC versus untreated
Culture age [DIV]
E
Puromycin
RM-CAMK2A
RM-Dlg4
RM-Ntrk2
F
Exc. synapse density
APV
MPX
G
RM-Grin2a per FOV
APV
Untreated

Figure 6: Combined Live-mRNA-PRISM Bayesian network and its chemical perturbations. A) Sequential images of the same fields of view with three timepoints of Fluo-8FF, one of the RIBOmap-PRISM rounds, and one of the Protein-PRISM rounds. Top row from untreated culture, bottom row for culture after chronic NMDAR blockade with APV. Scale bar is 10um. B) Inferred combined Bayesian network of eight protein, four translation and two activity variables, shown as a heatmap of edge strengths. Edges symmetric around the diagonal indicate unknown edge direction. C) Glutamate and calcium activity measurements of DIV 14 cultures over one hour after removal of chronic NMDAR inhibition with APV or NR2A-specific inhibition with MPX-004. Top: Number of glutamate spikes recorded in individual wells. Bottom: Synaptic calcium levels over time. The red line indicates average across all synapses while the grey shading denotes the 10th-90th percentiles. D-F) Changes to average synaptic levels of proteins (D), translation indicators by puromycin incorporation and RIBOmap-PRISM (E) and excitatory synapse density (F) one hour after removal of chronic treatments in DIV 7, 10 and 14 cultures. Log_2-FC relative to untreated cultures. G) Number of somatic Grin2a RIBOmap-PRISM puncta per field of view in untreated and APV-treated DIV 14 cultures. Error bars are mean ± sem across wells

DIV 10 but otherwise stable, including at DIV 14, where we observed a reduction in *Grin2a* translation as measured in counts of RIBOmap-PRISM puncta of the gene (Fig. 6g). We also observed, as we have previously[31], a strong increase in the amount of AMPAR and/or NMDAR-positive synapses (Fig. 6f).

Utilizing the multiplexed nature of our measurements, we looked to see how the effects on each protein or translation measure change when controlling for each of the other proteins, at DIV 14 (Fig. S4b). We observed that despite the moderate increase in NR2B (compared to increases in other markers), controlling for it attenuated the effects on most other proteins, indicating its potential causal connection (upstream or downstream) in the processes changing other protein levels. Effects were also attenuated by controlling for CaMKIIα, which may be an artifact of this protein showing the strongest increase. NR2A levels were reduced when controlling for other proteins, indicating that their increase may be necessary for maintenance of NR2A levels despite globally reduced expression.

Because the three time points had cultures both at different ages (DIV 7,10,14) and treated for different times with APV (2, 5 and 9 days), we wanted to compare the effect with same-age (DIV 19) cultures treated with APV for 2, 8 and 14 days prior to removal of the drug, and full multimodal calcium-mRNA-multiprotein imaging (Fig S4c-d). These showed similar increases in synaptic proteins and mRNA translation, albeit weaker (possibly an artifact of using the calcium indicator/buffer after removal of the drug) and with an overall decrease in NR2A. Translation of *Actb* was not affected, indicating a preference for synaptically translated genes, and the effects on starting synaptic calcium and calcium end-to-start ratio were as above, with effects increasing in strength with longer APV treatments. We also measured how the Bayesian network edges changed under treatment with APV (Fig. S5d-e). We observed edges leading to NR2A were stable despite changing levels of the protein. Conversely, edges leading to CaMKIIa were weakened, indicating a perturbation of unmeasured mechanisms that regulated its synaptic levels. Overall, affected and unaffected edges were congruent with changes in protein levels vis-à-vis predictions from the Bayesian network. That is, if the response of a protein differed from its prediction relative to NR2A, that indicated a perturbation in the mechanism regulating it, which could be observed in changing edge strengths.

To test whether these effects may be due to decreased NR2A function, rather than expression , we compared in parallel the effects of chronic NR2A-specific antagonism with MPX-004[65] (Fig. 6c-d, S4b). Chronic NR2A-specific antagonism showed glutamate potentiation (Fig. 6c), but weaker and largely opposite, at DIV 14, effects on synaptic calcium traces, proteins, mRNA translation, and excitatory synapse density (Fig. 6d, S4b), especially on CaMKIIα. Like with APV, these effects were attenuated most when controlling for NR2B and CaMKIIα. Synaptic NR2A was decreased under APV and increased under MPX-004 at DIV 10, which may indicate that both long-term responses are downstream of NR2A abundance rather than specific NMDAR subunit activity, although comparison with NR2B-specific antagonists and lower APV concentrations will help elucidate activity-dependent effects.

We were interested in the causal dependencies between the effects on synaptic proteins and activity. We observed that the effect of APV on CaMKIIa was attenuated when controlling for changes in calcium trajectory (Fig. S5d) but not the reverse, indicating that CaMKIIa increase is likely dependent on the calcium increase, as predicted by the Bayesian network. A plausible mechanism can be calcium intake-dependent autophosphorylation recruiting receptor subunits such as NR2B which have binding spots for further CaMKIIa units[66], as well as stimulating local synaptic translation. To directly test this prediction along with our assumption that observed calcium increase depends on spiking activity, we measured calcium dynamics, glutamate spiking, and CaMKIIa in cultures chronically treated with APV and then imaged for 1hr under TTX and fixed ("APV→TTX"), to cultures chronically treated with APV and then imaged for 1hr without chemical perturbation, as performed in figure 6 ("APV→Ø") (Fig. 7a). As anticipated, TTX prevented the potentiation in spike intensity and overall culture activity seen by the APV→Ø treatment relative to untreated cultures. This in turn prevented the increased calcium ratio and attenuated the increase in CaMKIIa. However, longer-term changes occurring under chronic APV treatment, such as the reduction in starting calcium levels and increase in excitatory synapse density, were independent of recent culture activity.

If changes in synaptic composition under chronic APV were due to reduced global expression of NR2A, similar effects should be observed from partial knockdown or knockout of *Grin2a*. Loss of function genetic mutations in *Grin2a* expression are highly penetrant for schizophrenia[67], for which a knockout mouse model exhibits considerable face validity[68]. We thus sought to investigate whether the predictions for *Grin2a* depletion made by the Bayesian network would extend to molecular changes in this model, translating across species, brain regions, and mode of perturbation. We plated cortical neurons from litter-matched *Grin2a*+/- ("Het") and *Grin2a*+/+ ("WT") mouse pups, grown and fixed at DIV 6 or DIV 14. We then performed PRISM staining and imaging for eight synaptic proteins as well as puromycin incorporation, measuring, as before, overall changes to each synaptic marker (Fig 7b) as well as changes when controlling for other markers (Fig. S6c).

We observed results similar to those induced by APV and to our prior observations with *Grin2a* RNAi[31], with the difference that some changes were transient and others cumulative: a transient increase in synaptic NR2B, PSD95 and puromycin, and cumulative or sustained increases in GluR2, CaMKIIa, F-actin and Bassoon, as well

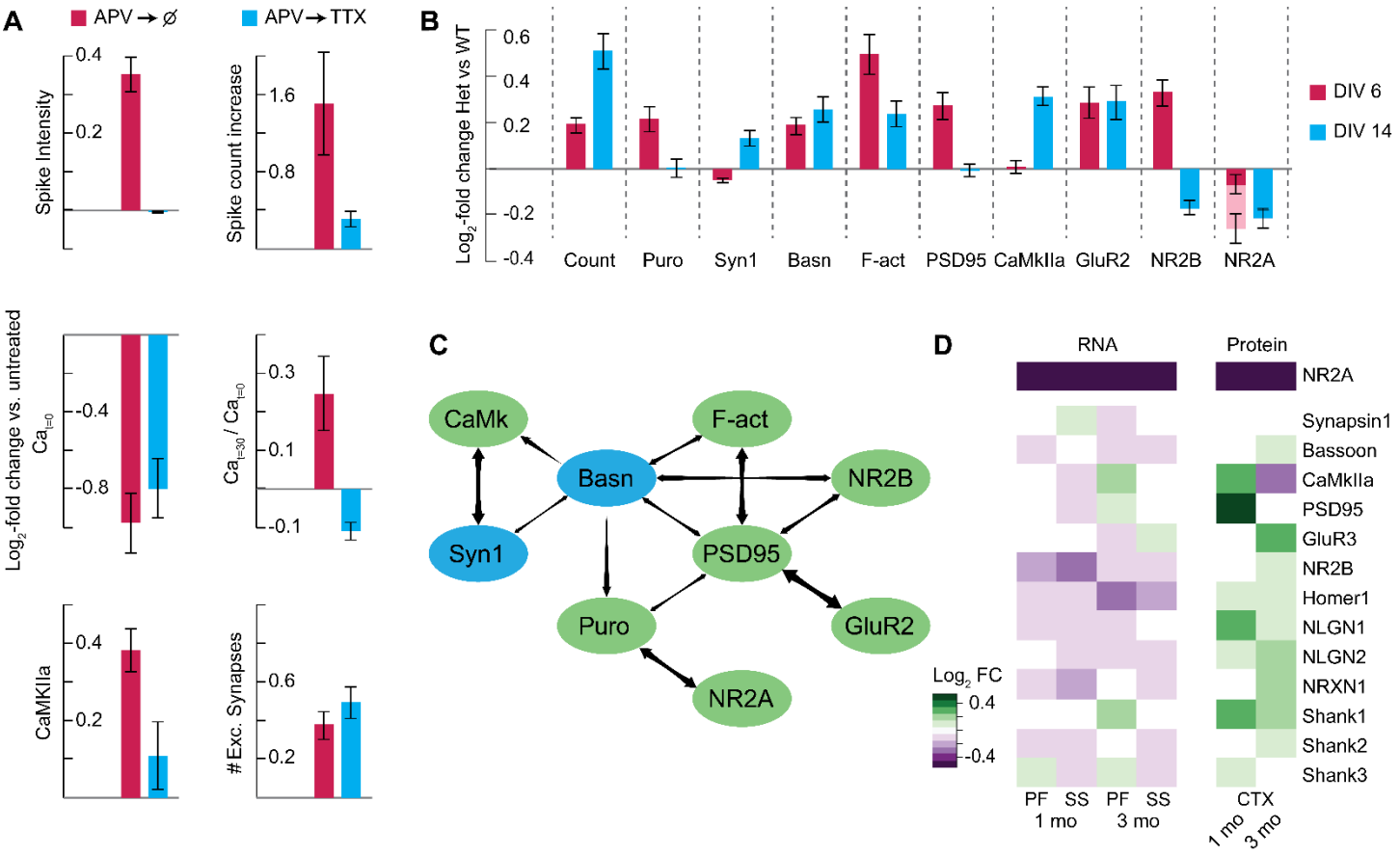
A
APV → ∅
APV → TTX
Spike Intensity
Spike count increase
Log2-fold change vs. untreated
CaMKIIa
Exc. Synapses
B
Log2-fold change Het vs WT
DIV 6
DIV 14
Count
Puro
Syn1
Basn
F-act
PSD95
CaMkIIa
GluR2
NR2B
NR2A
C
CaMk
F-act
Basn
NR2B
Syn1
PSD95
Puro
GluR2
NR2A
D
RNA
Protein
Log2 FC
Synapsin1
Bassoon
CaMkIIa
PSD95
GluR3
NR2B
Homer1
NLGN1
NLGN2
NRXN1
Shank1
Shank2
Shank3
PF
SS
1 mo
3 mo
CTX

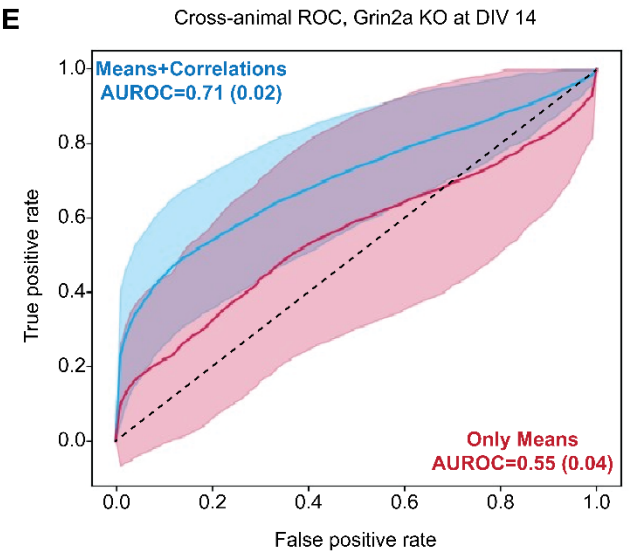
E
Cross-animal ROC, Grin2a KO at DIV 14
Means+Correlations
AUROC=0.71 (0.02)
Only Means
AUROC=0.55 (0.04)
True positive rate
False positive rate

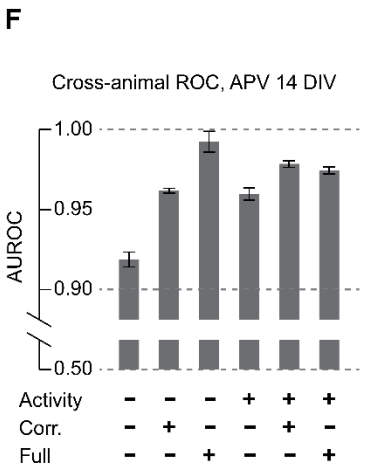
F
Cross-animal ROC, APV 14 DIV
AUROC
Activity
Corr.
Full

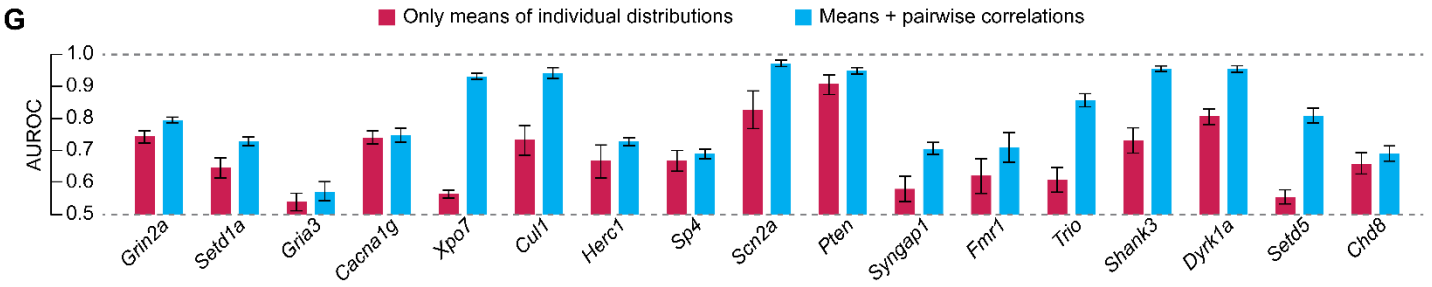
G
Only means of individual distributions
Means + pairwise correlations
AUROC
Grin2a
Setd1a
Gria3
Cacna1g
Xpo7
Cul1
Herc1
Sp4
Scn2a
Pten
Syngap1
Fmr1
Trio
Shank3
Dyrk1a
Setd5
Chd8

Figure 7: A) Log_2-Fold changes in two treatments compared to untreated cultures in (i) mean glutamate spike intensity, (ii) ratio of spike counts at T_0 + 45min to spike counts at T_0, (iii) mean starting calcium levels at T_0, (iv) ratio of mean calcium levels at T_0+30min to mean levels at T_0, (v) mean synaptic levels of CaMKIIa, (vi) active excitatory synapse density (synapses positive for GluR2).
B) Average synaptic protein levels, as well as overall excitatory synapse density and synaptic puromycin signal, in Grin2a +/- neurons grown to DIV 6 and 14, shown as Log2-FC relative to neurons from +/+ pups from the same litter. Pink and light blue NR2A columns indicate Log-fold change of NR2A when controlling for all other synaptic proteins (methods).
C) Bayesian network of nine synaptic variables in mouse cortical neurons, merged from networks inferred from DIV 6 and DIV 14.
D) Changes to bulk cortical RNA and protein levels of synaptic genes in Grin2a +/- mice at one and three months of age, Log2-FC relative to litter-matched wild-type mice.
E) ROC curves and areas (AUROC) from SVM models trained on data from DIV 14 neurons of three heterozygous and two wild-type embryos and tested on data from the other two heterozygous and one wild-type embryo (Methods). Traces and margins are average curves and standard deviations across all 30 permutations of train-test data split. The red curve is from SVM models using only separate protein/puromycin means in each synapse cluster datapoint (see Methods for definitions). The blue curve is from SVM models using both protein means and pairwise correlations from each datapoint.
F) AUROCs from SVM models trained on data from one APV perturbation Live-multiprotein experiment and tested on data from a separate experiment that used a different animal. All models used mean protein levels and either did or did not incorporate (i) calcium level traces, (ii) pairwise correlations, (iii) the entire synapse cluster distribution.
G) AUROCs from SVM models trained on siRNA-mediated knockdown data (versus cultures treated with nontargeting siRNA). Models were trained on data from two plates and tested on the two other plates. Each plate contained mixed neurons from 1-3 embryos of a separate pregnant rat.
E-G AUROCs and errors indicate average and s.e,m. across all possible permutations of training and test data.

as in the density of excitatory synapses. Interestingly, the reduction in synaptic NR2A levels was small (~10%) and insignificant. We observed a similar robustness in *Grin2a* RNAi of rat hippocampal neurons, where synaptic NR2A levels were unchanged despite up to 50% reduction in Grin2a translation events identified by RIBOmap (Fig. S6a-b). We also observed in Grin2a RNAi a similar transient increase in NR2B and cumulative increase in CaMKIIa as in the knockout model. Together, these observations reinforce the notion that synaptic NMDAR levels are strongly regulated by a local synaptic mechanism that responds to NR2A protein deficiency with increased synaptic translation and potentiation. We constructed the nine variable Bayesian network of synaptic markers in mouse cortical neurons (Fig. 7c). We observed an overall similar structure to the networks we constructed from various datasets in rat hippocampal neurons, including the Bassoon-F-actin-PSD95 triangle, and the causal dependencies between PSD95 and AMPARs and NMDARs. We also measured a relatively strong edge between puromycin and NR2A, supporting the direct dependence between synaptic translation and NR2A levels.

To test whether these observations and predictions applied *in vivo*, we measured bulk RNA and synaptosome protein levels (Methods) of several synaptic proteins in cortices of one- and three-month-old litter-matched wild-type and heterozygous Grin2a knockout mice (Fig. 7d). We observed an approximately 2-fold decrease in NR2A protein and RNA levels, and increases in numerous excitatory postsynaptic proteins including PSD95, CaMKIIa, GluR2, and NR2B, as well as others not measured in multiplexed imaging, which likely stems from some combination of increased excitatory synapse density and potentiation. We also observed that many of these proteins have unchanged or even decreased RNA levels, consistent with a regulatory response at the translation level.

Importantly, when grouping the Grin2a +/- and +/+ cultures by the specific embryo they came from (five heterozygous knockout and three wild-type embryos), we observed significant differences between individual animals in average protein and puromycin measures. Accordingly, when training an SVM[40] classifier (Methods) only on average protein levels in synapse distributions from one set of animals, the model had essentially no predictive ability to discern knockout from wildtype animals in the test set (AUROC: 0.55±0.04, Fig. 7e, red curve). However, this predictive ability significantly increased when incorporating protein-protein correlations (AUROC: 0.71±0.02, Fig. 7e, blue curve). Even with the chronic APV treatment phenotype, which is stronger and more robust across animals (AUROC >0.9), including correlations or full multiprotein distribution data increased between-animal predictive ability even further, as did incorporation of live imaging data (Fig. 7f). Finally, we used this observation to revisit our dataset of multiprotein synaptic imaging under RNAi knockdown of autism- and schizophrenia-associated genes. Here too we observed that incorporating protein-protein correlations significantly increased between-animal predictive ability of SVM classifiers for many tested genes (Fig. 7g). Together, these observations indicate that multimodal synapse distributions encode phenotypes that are more consistent across individual animals than separate bulk measurements of proteins.

Discussion

We present a modular and versatile multi-modal method to acquire simultaneous information about live activity, biochemical processes and multiprotein compositions of subcellular molecular systems. We expect our approach to be generalizable to most systems, such as phagosomes or endosomes, which can be identified and automatically segmented into individual organelles or subcellular regions in fluorescence micrographs, as we have demonstrated here in synapses and mitochondria.

Beyond CAT- and GRL-PRISM, other methods of Live-PRISM can employ other indicators such as genetically encoded calcium indicators[8,69-71], which can be targeted to pre- or postsynaptic compartments and expression tuned to minimize buffering artifacts. It can also be used for other targets for which single-synapse zsensitive sensors exist, such as catecholamines[72]. It can be replaced or combined with activity integrators, such as SynTagMA[73]. Expanding to other systems one can use fluorescent tags to track organelle movement/morphology, as well as other activity variables as relevant, such as membrane[74], pH[75] or redox[76] potentials or chemical output[77]. Our method for incorporating RIBOmap into PRISM can be adapted to any detection mechanism for molecular processes that outputs a DNA strand, either as an RCA amplicon or otherwise. These include STARmap for spatial transcriptomics[78], proximity ligation assay for interactions of proteins with other proteins[79], with RNA[80], or of nascent peptides with incorporated puromycin[81], and transposon-based imaging methods such as ATAC-see for nuclear[82] or mitochondrial[83] chromosome accessibility. This generalizability is assisted by the fact that simple fluorescent optics are mostly sufficient for Multimodal-PRISM data generation, with spinning disk confocal and rapid scanning systems employed here used to boost sensitivity and throughput.

It is important to note certain limitations in interpreting data from different modalities. First, RIBOmap-PRISM reports on mRNA-protein associations, which can occur in the absence of translation, for example as

static polysomes, including in synapses[35,84,85]. We thus refer to RIBOmap-PRISM puncta, although they correlate with puromycin incorporation, as putative translation events. Second, Live-PRISM imaging occurs in tandem and not in parallel, so the resulting data combines protein and mRNA levels at the time of fixation with activity information from one hour leading up to fixation.

This novel kind of data, namely large multimodal distributions of synapses in high-dimensional space, requires analytical approaches not previously applied to single synapses. Here we used Bayesian network inference as an unbiased approach to represent the shape of high-dimensional distributions in terms of conditional distributions, which does not require prior assumptions about individual variable distributions or their relationships, although the latter can be incorporated. Network inference yields predictive information about relationships between variables, whether they are driven by physical protein-protein or protein-mRNA interactions, sequential reactions in phosphorylation cascades, or stoichiometric control. It can also identify subtle responses to chemical or genetic perturbations in unmeasured variables via their effects on the controlled correlations between measured variables, providing a rich phenotyping platform as observed previously[31].

That said, Bayesian network inference, and particularly inference of edge directionality, is sensitive to data noise and thresholding of edge strengths. Thus, while the network can generate hypotheses about causal connections between nodes, these must be tested with direct perturbations as performed here and previously[31]. With additional prior assumptions in hand, such as a categorical difference between one variable (activity) and others, multivariate models like those applied here to glutamate live-PRISM data can be used to extract directly interpretable relationships.

Specifically, we applied this approach to study synaptic response to changes in NR2A levels and activity, which is central to nominal brain function, to understanding the effects of schizophrenia genes, and response to NMDAR-active compounds such as ketamine. We discovered a wide range of processes occurring in synaptic activity and protein synthesis and localization. While much remains unknown about the causal dependencies between these processes, which can be addressed with targeted perturbative experiments, and some observations appear contradictory, such as the increased glutamate potentiation but decreased calcium potentiation under MPX-004, we can glean the following: Chronic global reduction of NR2A expression, either genetically or chemically induced, leads to synaptic potentiation seen in increased synaptic proteins, local translation of synaptic genes, and stronger accumulations of calcium (from a lower starting point) and increases in glutamate spiking. Because NR2A-specific antagonism leads to a very different and largely opposite response, we hypothesize that this potentiation is a response to reduced NR2A presence rather than activity. This potentiation is a combination of multiple processes, and high-dimensional imaging allows dissection of some causal dependencies between them, for example the centrality of NR2B accumulation, and the dependence of the increase of CaMKIIa on potentiated activity.

Bayesian network inference and regression analyses from multimodal imaging can predict some of these processes. Direct edges between NR2A and puromycin or S6RP indicate its dependence on local synaptic translation of other proteins (and predict its mTORC-dependent response to BDNF stimulation) which is increased to maintain local NR2A levels in response to global depletion. Negative edges and regression coefficients between NR2A (or NR2B-controlled NR1) and GluR2, CaMKIIa, glutamate spiking, and calcium

increase predict that a local decrease in NR2A would lead directly to an increase in both GluR2 and glutamate spiking and vice versa. This may occur via changing silent synapse populations. Thus, immediately after APV is removed synaptic calcium is lower but accumulates faster due to higher firing, and synaptic CaMKIIa increase seems to be dependent on this process.

Multimodal synaptomics achieved with Multimodal-PRISM is thus not only a phenotyping approach that reveals molecular changes inaccessible to other methods, but also a hypothesis generator to assist in the study of complex, compartmentalized and independently regulated subcellular systems.

Acknowledgements

This work was supported by NIMH R01-MH112694, NIMH R21-MH130624, and NSF-PoLS 1707999 awarded to M.B., as well as Effective Ventures grant and the TVML foundation fellowship awarded to R.F. The work was also supported by the Center for Discovery of Therapeutics at the Broad Institute and use of the PerkinElmer Opera Phenix high-content/high-throughput imaging system funded by the S10 grant NIH OD-026839-01, as well as by MIT CEHS core center grant P30-ES002109 from the National Institute of Environmental Health Sciences. S.A. and M.S. were supported by the Stanley Center for Psychiaric Research. The authors would also like to thank Xiao Wang and Rena Ren for assistance with RIBOmap, Anna Lapteva for assistance with invader strand design, Opalina Vetrichelvan for Bayesian network-related calculations, and Maria Alimova and Ranjith Muraleedharan for assistance with high-throughput imaging.

Supplementary Information

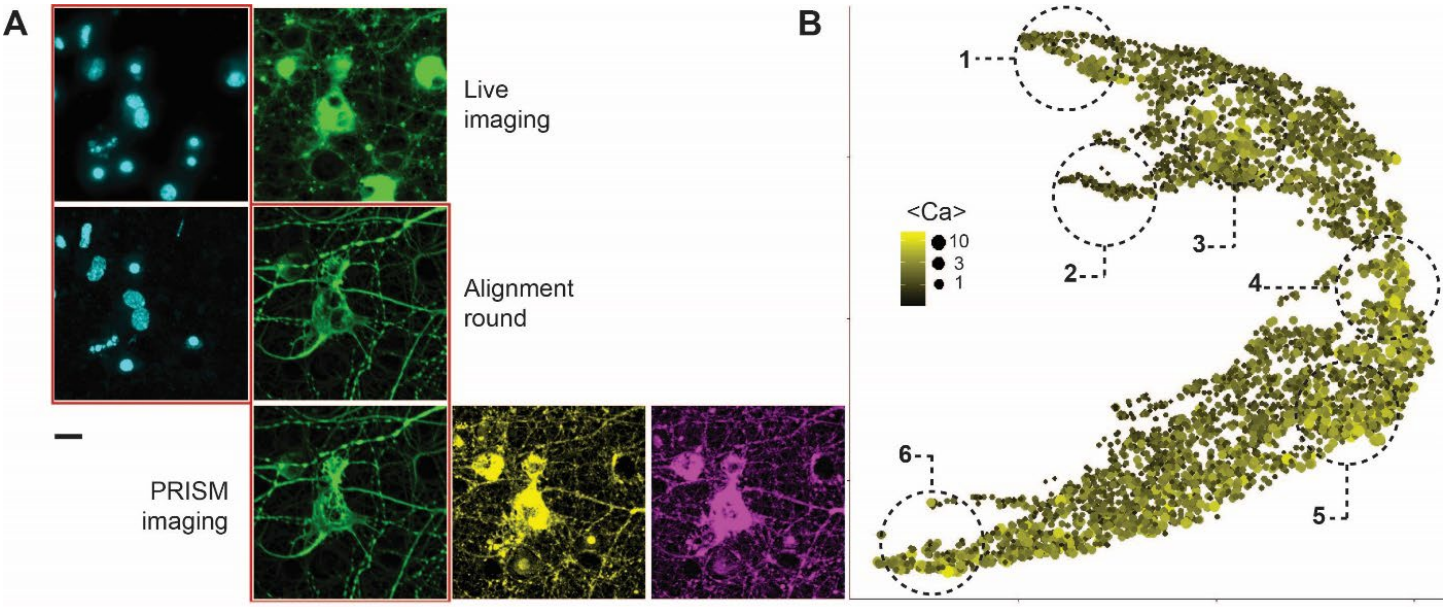

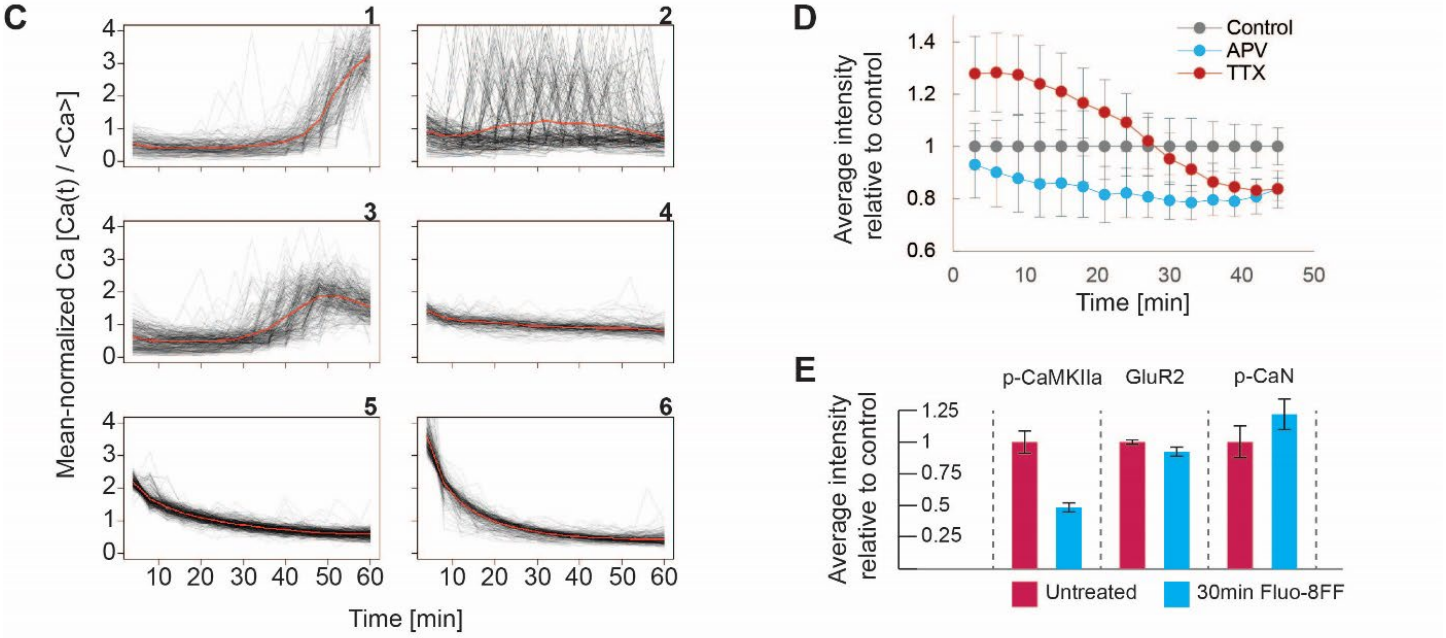

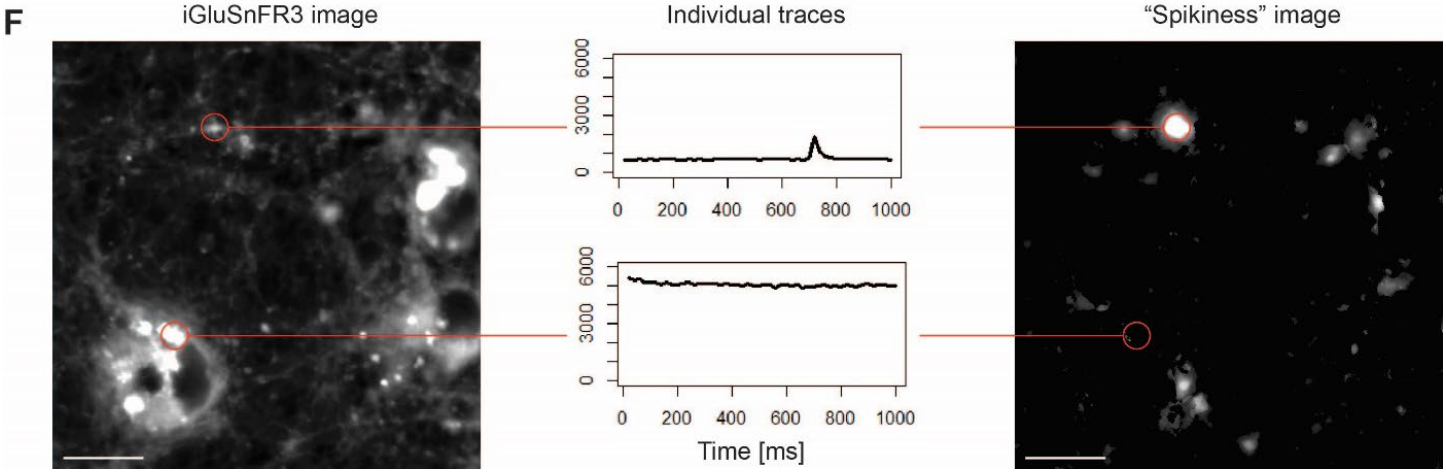

Supplementary figure S1: A) Live-PRISM alignment. Combined Hoechst and calcium imaging is aligned via the 405nm Hoechst channel to a post-fixation alignment round, which in turn is aligned to all PRISM imaging rounds via the 488nm MAP2 channel. B) UMAP of synaptic calcium trace shapes (from distances assigned by DTW), colored and sized by average calcium signal. C) Individual (gray) and average (red) calcium traces in regions 1-6 circled in (B). D) Average synaptic calcium signal over time in APV- and TTX-treated synapses, relative to untreated synapses. Error bars indicate S.E.M. across wells. E) Average synaptic levels of phospho-CaMKIIa, GluR2, and phospho-Calcineurin, in neurons exposed to 10uM Fluo-8FF. F) Maximum projection across a representative exposure window in iGluSnFR3 imaging and its corresponding spike analysis image, with traces from a weak but spiking and a strong but nonspiking region highlighted. A,F scale bars are 10um.

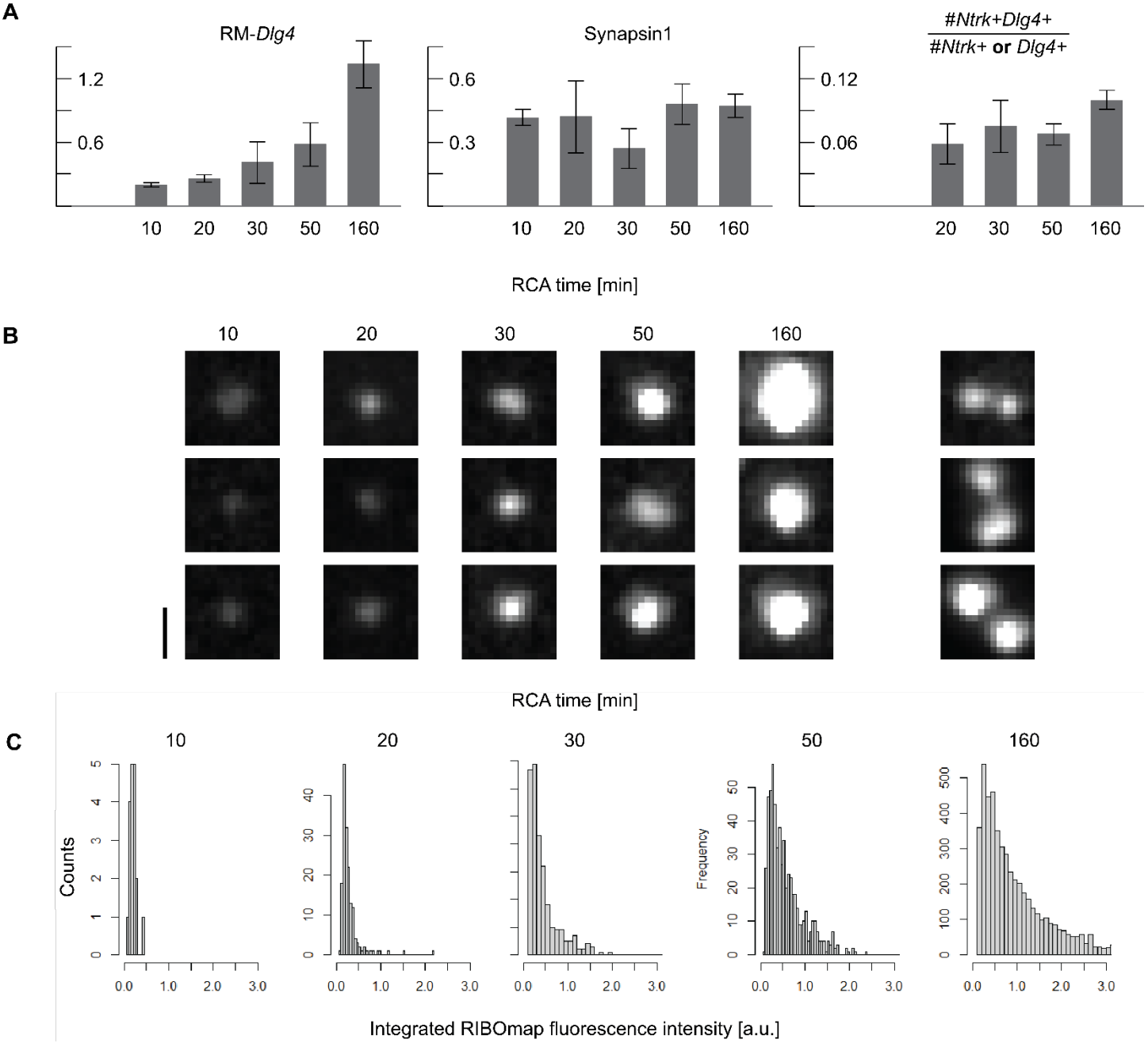

Supplementary figure S2. A) Left: Average *Dlg4* RIBOmap-PRISM intensity integral in synapses positive for *Dlg4*, in cultures that underwent different amplification times in the RCA step. Middle: Average Synapsin1 signal in *Dlg4*-positive synapses. Right: Fraction of puncta which are positive for both *Ntrk2* and *Dlg4*, out puncta positive for either. The 10-minute amplification time showed too few *Ntrk2*-positive puncta for a reliable estimate. B) Representative RIBOmap-PRISM puncta from different amplification times. Right column shows pairs of

adjacent puncta assigned to the same synapses which were segmented properly. C) RIBOmap-PRISM intensity histograms of *Dlg4* puncta in different amplification times.

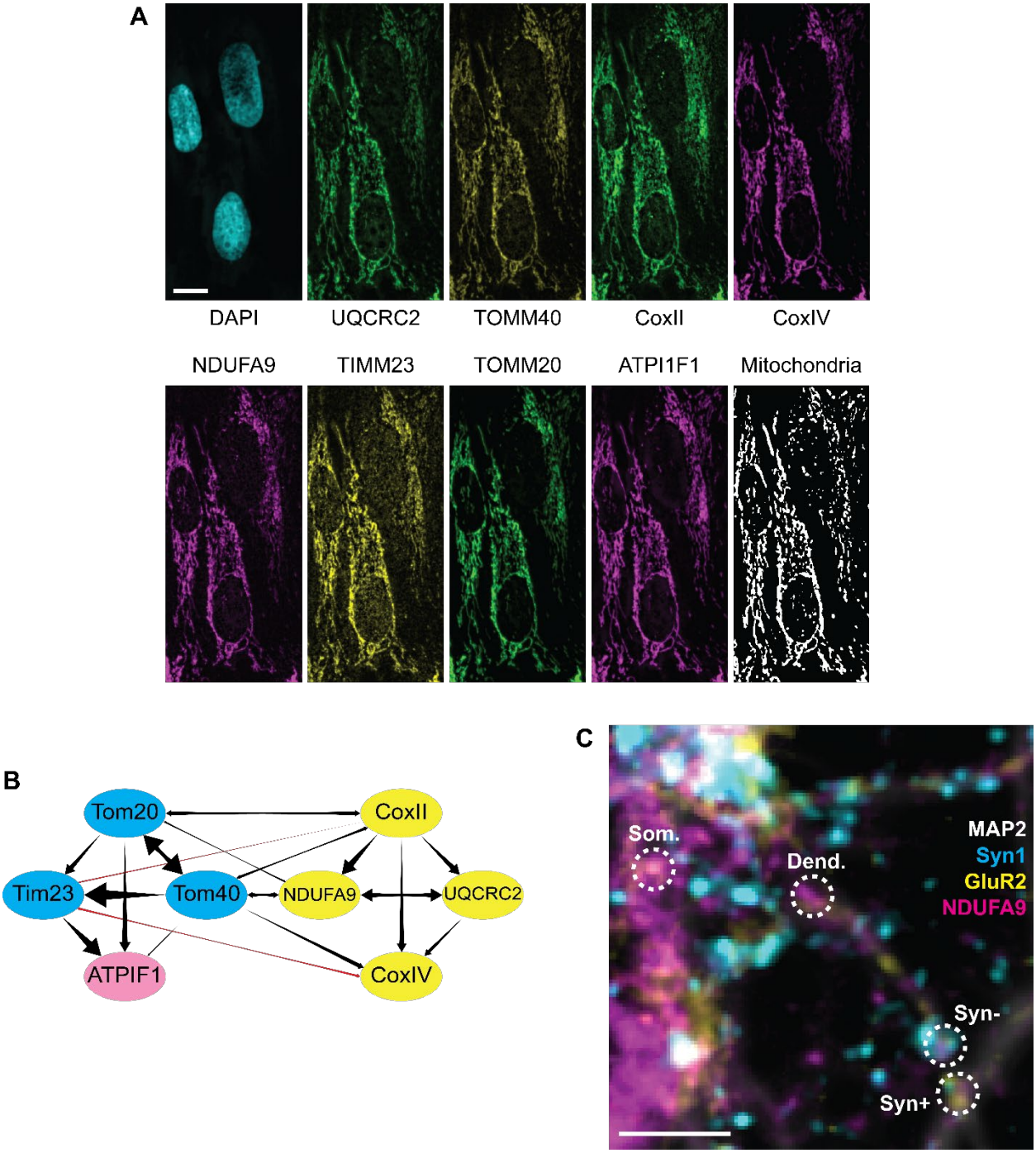

Supplementary figure S3. A) PRISM images of eight mitochondrial proteins, as well as DAPI and all ID'd mitochondrial area, in HeLa cells. Scale bar is 20um. B) Bayesian network of average protein levels in HeLa cells. C) Overlaid image of MAP2, Synapsin1, GluR2 and NDUFA9 in neurons, showing NDUFA9-ID'd mitochondria assigned as either somatic, extrasynaptic dendritic, and synaptic GluR2- or GluR2+. Scale bar is 5um.

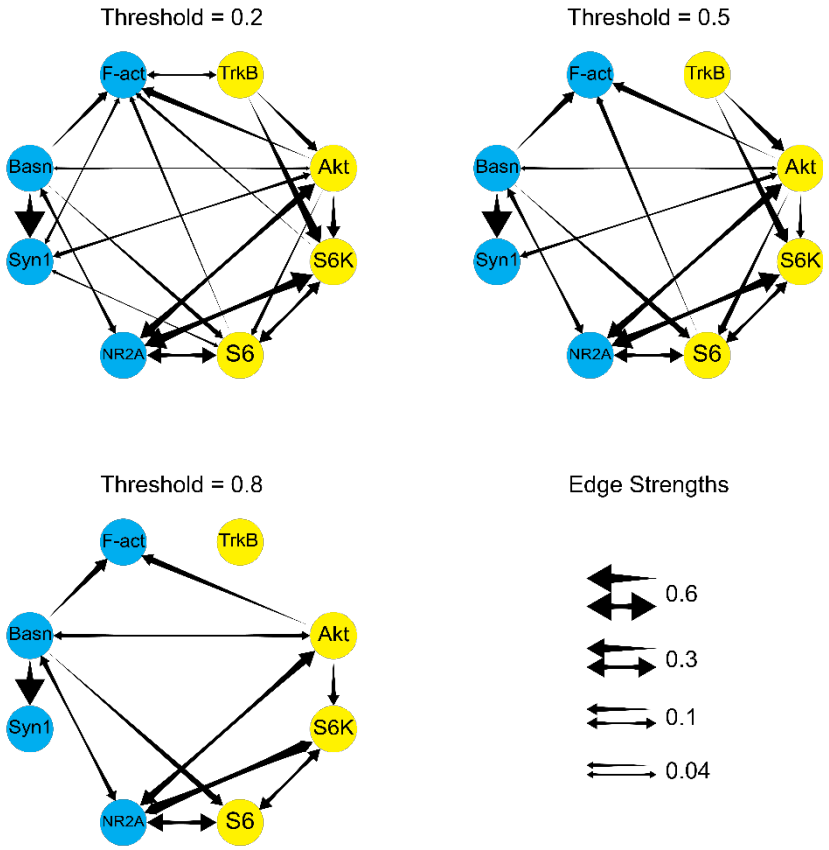

Supplementary figure S4: Bayesian network inference on the BDNF response pathway, calculated in untreated cultures. Networks are shown at three levels of thresholding on the bootstrapped edge frequency (see Methods).

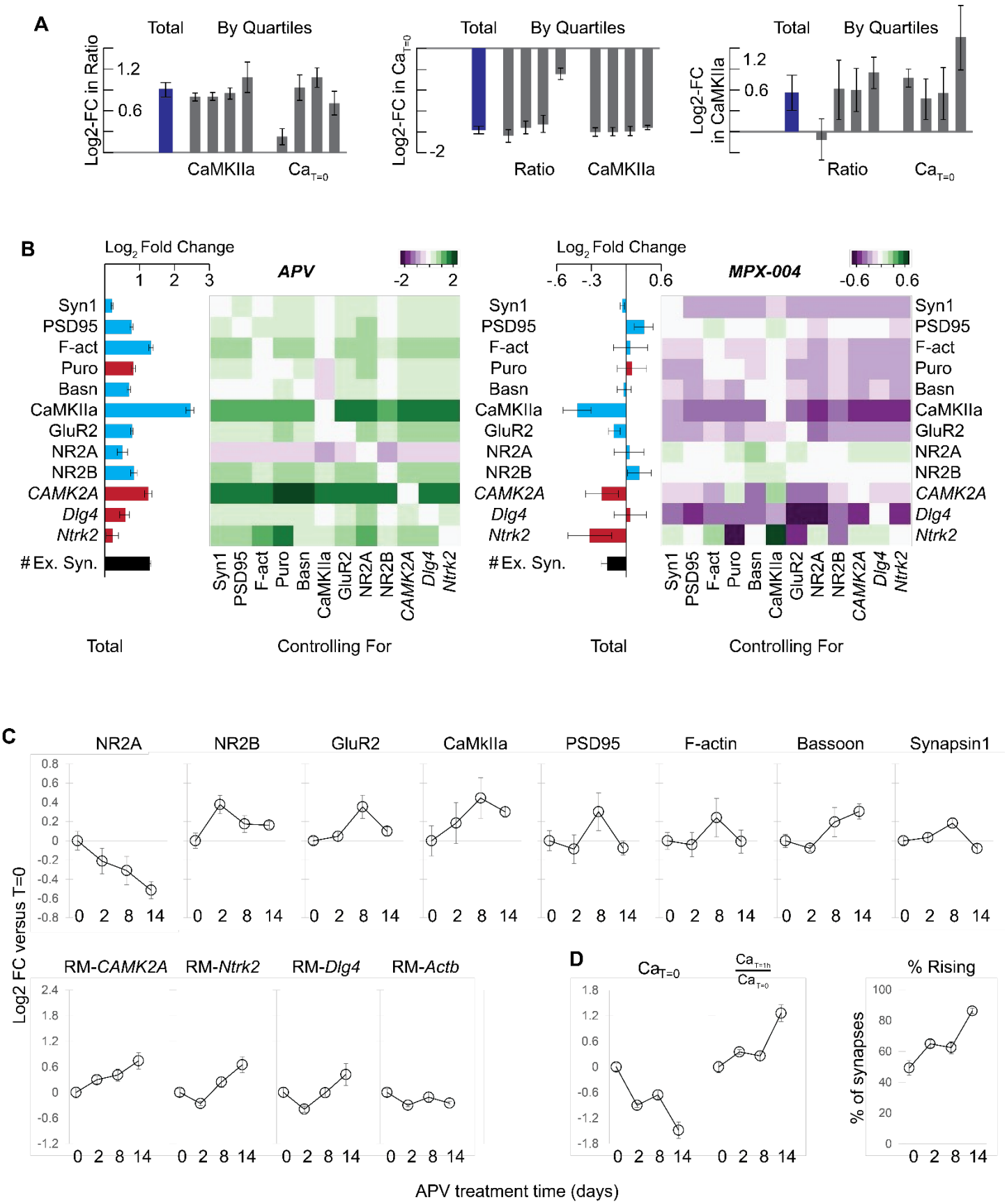
A
Total
By Quartiles
Log2-FC in Ratio
1.2
0.6
CaMKIIa
Ca$_{T=0}$
Log2-FC in Ca$_{T=0}$
-2
Ratio
Log2-FC in CaMKIIa
B
Log$_2$ Fold Change
APV
MPX-004
Syn1
PSD95
F-act
Puro
Basn
CaMKIIa
GluR2
NR2A
NR2B
CAMK2A
Dlg4
Ntrk2
Ex. Syn.
Total
Controlling For
C
NR2A
NR2B
GluR2
CaMkIIa
PSD95
F-actin
Bassoon
Synapsin1
Log2 FC versus T=0
RM-CAMK2A
RM-Ntrk2
RM-Dlg4
RM-Actb
D
Ca$_{T=0}$
Ca$_{T=1h}$ / Ca$_{T=0}$
% Rising
% of synapses
APV treatment time (days)

Supplementary figure S5: A) Log_2-fold changes in average synaptic calcium increase ratio (left), starting calcium level (middle), and CaMKIIa (right), over all synapses and broken up by quartiles of the other two measurements. Error bars are S.E.M. across wells. B) Average synaptic levels of proteins at DIV 14 (log-FC relative to untreated) one hour after removal of chronic treatments (Fig. 6d). Overall averages (left bars) and when controlling for each of the other proteins (heatmap). C) Changes to protein levels and translation indicators in DIV 19 cultures treated for 2, 8 and 14 days with APV (relative to untreated, denoted here as time 0) before one-hour calcium imaging and fixation. D) Changes to starting calcium levels, average calcium ratio, and percent of synapses with a higher calcium signal after an hour compared to at start.

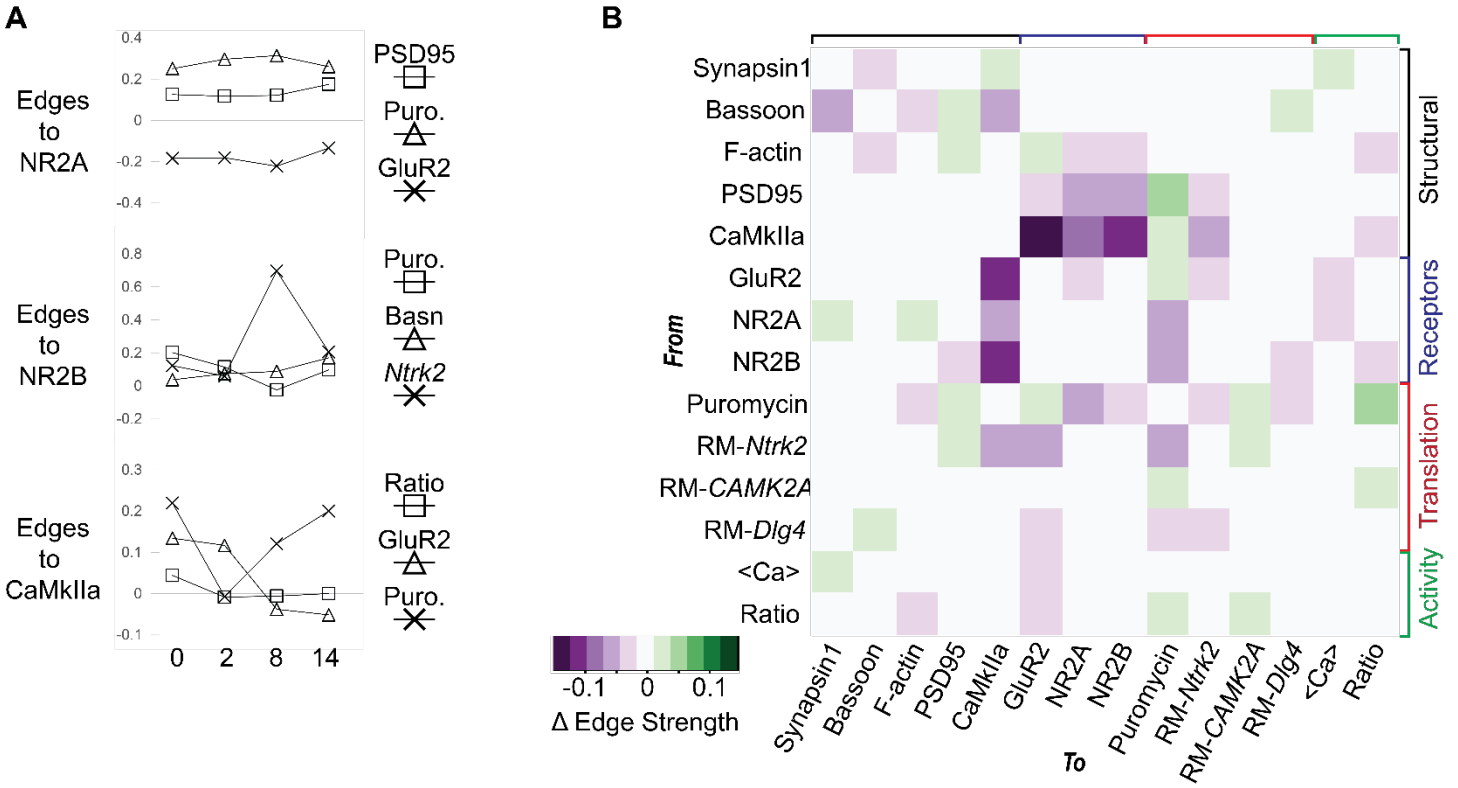

Supplementary figure S6: Changes to the synaptic Bayesian network in Fig. 6b under APV treatment. A) Strength of select network edges in untreated (0) and 2, 8 and 14-day APV treated cultures. B) Absolute change to all the network edge strengths at 14 days of APV treatment.

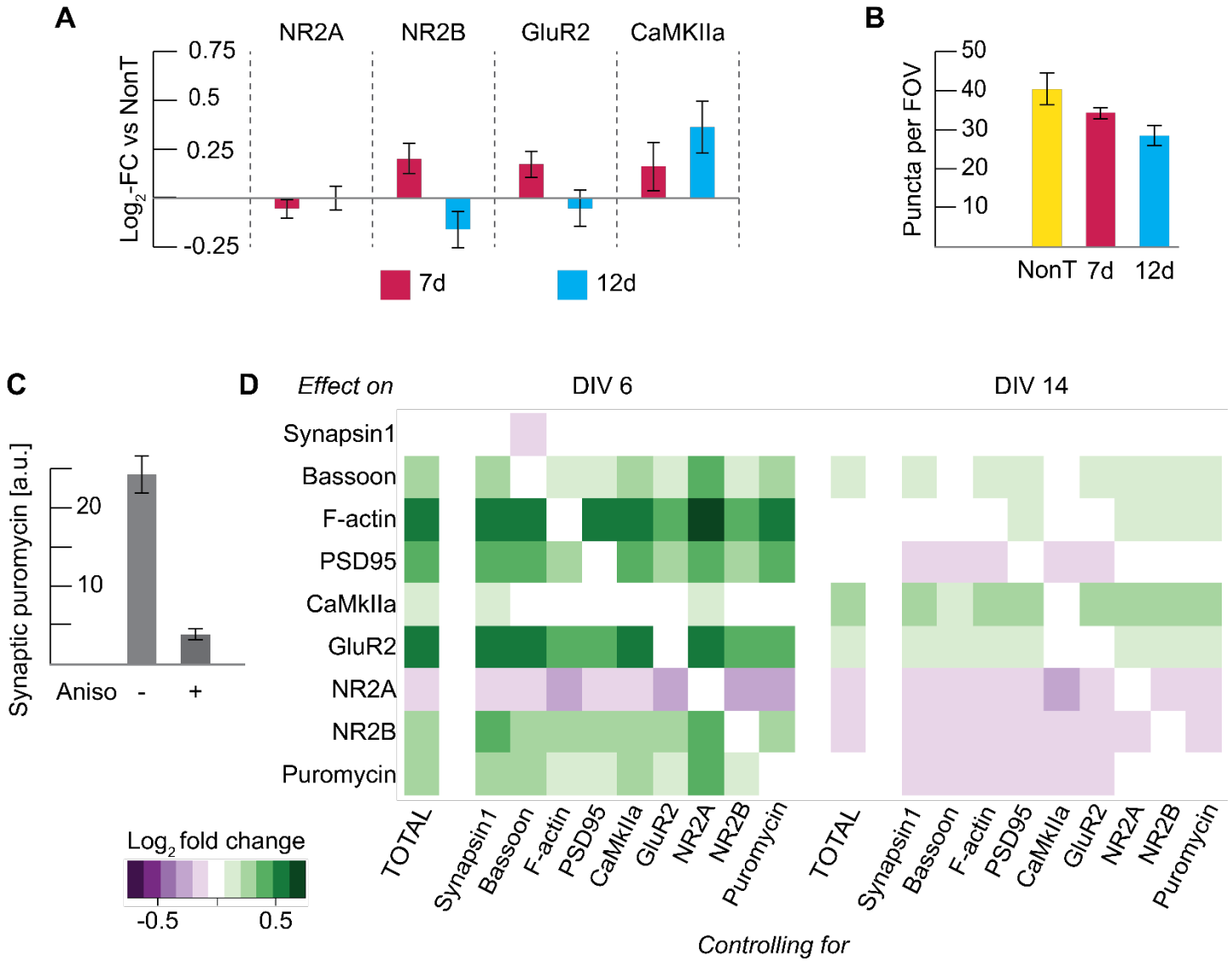

Supplementary figure S7: A) Log2-fold changes to average synaptic protein levels in culture treated with self-transfecting siRNA against Grin2a (relative to treatment with nontargeting siRNA) for 7 or 12 days before fixation at DIV 18. B) Grin2a RIBOmap-PRISM puncta density in the different treatment groups. C) Average synaptic puromycin levels with and without pretreatment with anisomycin before puromycin labeling. D) Log2-fold changes in each marker, total and controlling for all other markers, in neurons from Grin2a+/- versus Grin2a+/+ mice.

Methods

Orthogonal imaging-docking sequence pair generation

Sequences 1-12 were identical to those previously published[27] except LNA imaging strands were extended with a 5' four-nucleotide toehold (ACTC) for toehold-mediated strand displacement by invader strands (see below). Additional sequences (13-29) were generated by screening a randomly generated library of 11-nt docking strands with GC content between 10 and 30% against existing LNA imaging strands using our previously published algorithm for crosstalk prediction[27]. Lowest scoring sequences were converted to 15-nt LNA imaging strands with all possible variations on locked base positions and screened against all existing and new DNA docking strands. This generated 17 docking-imaging pairs with low predicted crosstalk scores against each other and published sequences. Crosstalk was tested experimentally by binding biotinylated docking strands to a streptavidin-coated plate (ThermoFisher) and measuring fluorescent LNA signal after probe binding and washing as described below. Two sequences were removed after exhibiting some crosstalk with existing sequences. Another sequence was removed after testing for nonspecific binding to unstained, RNase-treated neurons. This resulted in 14 new sequences of which seven were used alongside previously published ones.

Imaging reagent preparation

Antibody-DNA conjugates were prepared with either chemical (SMCC) or enzymatic (SiteClick) conjugation as described previously. Table S1 details the antibodies used for multiplexed imaging, including the conjugation strategy used for each. Table S2 details sequences of docking strands, imaging strands, invader strands, and RIBOmap probes.

Chemical conjugation was done using 4-(N-Maleimidomethyl)cyclohexane-1-carboxylic acid N-hydroxysuccinimide (SMCC), a heterobifunctional molecule which binds exposed amines on the antibody via an N-hydroxysuccinimide (NHS) moiety on one end and binds thiol-oligonucleotides via a maleimide on the other end. Antibodies were purchased as formulations without serum proteins as listed below (Table S1), 0.1-1 mg of antibody were purified into PBS and concentrated to 1 mg/ml using Amicon Ultra centrifugal filters (10 kDa, EMD Millipore). From a freshly prepared stock at 2 mM in DMF, SMCC (Sigma Aldrich) was added to the antibody at 7.5x molar excess. The reaction mixture was protected from light and incubated for 3 h at 4°C on a shaker. Excess SMCC was removed by purification into PBS using the above Amicon centrifugal filters.

In parallel, 25 nmol 5' thiol-modified ssDNA (Integrated DNA Technologies, modification catalog no. /5-ThioMC6-D/) were deprotected by mixing with 150mM DTT in 0.5x PBS, protected from light and incubated for 2 h at 25°C on shaker. The reduced 5′ thiol-modified ssDNA was purified into water using NAP-5 columns (GE Life Sciences). The reduced 5' thiol-modified ssDNA was spin vacuum dried, resuspended in 50ul water and added to the antibody-SMCC conjugate at 15x molar excess, the reaction mixture was protected from light and incubated overnight at 4°C on a shaker. Antibody-ssDNA conjugates were purified into PBS using Amicon Ultra centrifugal filters (10 kDa, EMD Millipore). Amino-modified phalloidin (Bachem) was conjugated using the procedure described above, but with the following changes: the molar excess of SMCC was 10x and the molar excess of reduced 5' thiol-modified ssDNA was 1x. HPLC purification was employed to remove unreacted SMCC and 5' thiol-modified ssDNA, respectively (Waters, BEH C18 column, gradient for phalloidin-SMCC: from 80% TFA in water and 20% acetonitrile to 20% TFA in water and 80% acetonitrile over 10 min, gradient for phalloidin-ssDNA: from 90% 0.1 M TEAA in water and 10% acetonitrile to 60% 0.1 M TEAA in water and 40% acetonitrile over 10 min). Antibody concentrations were determined by absorbance measurements at 280 nm.

Enzymatic conjugation was done using the SiteClick™ (Invitrogen) conjugation technique following the manufacturer's protocol. This technique replaces the Fc galactoses on the antibody with azide-modified sugars, which then react with a DBCO-modified oligonucleotide. 0.1-0.2mg of antibody are concentrated to 1-2 mg/ml in 1x Tris buffer and incubated with β-galactosidase. Azide-modified, terminal galactosides were attached using β-galactosyltransferase. Azide-modified antibody was purified into 1x Tris buffer using Amicon Ultra centrifugal filters (50 kDa, 4000 g, EMD Millipore).

In parallel, DBCO-modified docking strands were prepared by mixing 25nmol 5' amine-modified ssDNA (IDT) with a 20-fold excess of DBCO-NHS (Sigma-Aldrich) from a DMF solution, at 1:1 mix of DMSO and and PBS, for 3 hours at 25C. Excess DBCO was removed by 2x purification on NAP-5 columns and the conjugate was spin vacuum dried, resuspended in 50ul water and added to the azido-modified antibody at a 20-fold excess, then incubated for 48 hours at 4C. The conjugates were then purified from excess docking strand by repeated

concentrations on 30k MWCO Amicon centrifugal filter until the 260/280 ratio was stable. All antibody-ssDNA conjugates were stored at -20°C in PBS with 50% glycerol.

Imager strands: 5 nmol of 5'/3' diamino-modified ssLNA (IDT) was mixed 100 nmol of NHS-Alexa Fluor 568 or NHS-AlexaFluor 647 (Sigma Aldrich) in 1:1 PBS:DMSO. Following immediate vortexing, the reaction mixture was protected from light and incubated overnight at 25°C on a shaker. Excess dye was removed using NAP-5 columns (GE Life Sciences). Fractions containing ssDNA were identified using absorbance measurements at 260 nm. Subsequently, 0.1 M TEAA was added ssLNA-dye conjugates and conjugates bearing two dyes were purified by HPLC (Waters, BEH C18 column, gradient for Atto 565: from 80% 0.1 M TEAA in water and 20% acetonitrile to 70% 0.1 M TEAA and 30% acetonitrile over 10 min, gradient for Atto 655: from 90% 0.1 M TEAA in water and 10% acetonitrile to 75% 0.1 M TEAA in water and 25% acetonitrile over 10 min). Peaks corresponding to ssLNA conjugates bearing two, one or no dye were assigned based on absorbance spectra. Solvents were removed in vacuo and ssLNA-dye conjugates were dissolved in water to 5 to 20 µM, depending on the yield.

Rat embryonic neuron culturing and treatment

For all experiments except the Grin2a KO experiment, we used neurons from E18 embryonic rat hippocampus dissociated and plates as described previously. Hippocampi from embryos in separate pregnant Sprague Dawley rats were supplied by BrainBits LLC in Hibernate E, digested in Hibernate E containing 20 U/ml Papain (Worthington Biochem), and 0.01% DNase (Sigma-Aldrich) for 10 min at 37C and triturated. Neurons were spun down at 210g for 2x5min, cell pellets were then resuspended into NbActiv1+25uM glutamate (BrainBits LLC, now TransnetYX), and plated at a density of 22,000 cells/well onto poly-d-lysine-coated, black-walled, thin-bottomed 96-well plates (Corning BioCoat). After 24 hours, AraC was added to each culture at a concentration of 1uM, to suppress glia proliferation and minimize well-to-well variability resulting from it. At DIV 5 (or DIV 4 when drug treatment was started on DIV 5), the media was entirely replaced with preequlibrated NbActiv4 (BrainBits LLC) and subsequently maintained in this media. In experiments that involved puromycin labeling, 250nM puromycin (Sigma Aldrich) were added 15min before fixation. For anisomycin controls, puromycin labeling was performed after 30 minute pre-treatment of neurons with anisomycin (final concentration of 10 µg/ml).

Grin2a knockout neuron culturing

Female mice heterozygous for Grin2a (B6;129S-Grin2a<tm1Nak>, RIKEN BioResource Research Center) were paired with male wild-type (C57BL/6J, Jackson Labs 000664) mice. On embryonic day 16.5, a pregnant dam was euthanized by CO2 inhalation in accordance with the Institutional Animal Care and Use Committee guidelines. Pups (n=8) were surgically retrieved and the cortex of each pup was dissected out into ice-cold HBSS supplemented with glucose. The embryonic tissue was digested in 0.125% trypsin for 15 minutes (37 °C), triturated in ice-cold HBSS with a fire-polished glass pipette, and the resulting cell suspension passed through a 40 um filter. Cells from each pup were counted and plated on a black-walled clear-bottom poly-D-lysine coated 96-well plate (Corning) at a density of 20,000 cells/well (6 replicates per pup). Neurons were cultured in NbActiv4 medium (TransNetyx LLC) supplemented with penicillin/streptomycin in a 5% CO2 incubator at 37 °C. Cytosine arabinoside (Ara-C; 1 µM final concentration) was added at DIV1; media with Ara-C was discarded on DIV2 and fully replaced with fresh media. Neurons were supplemented with additional fresh media every 3-4 days.

CAT-PRISM

Neurons were treated at T-45min before imaging with 5uM Fluo-8FF (AAT Bioquest) and at T-10min with 10uM Hoechst 33342. At T=0, the media was replaced with pre-equilibrated BrainPhys Imaging Medium[86] (StemCell Technologies) containing any indicated chemical treatment and imaging started at approximately T+10min. Calcium imaging was performed as repeated minimal exposure confocal imaging in the 488 channel over the entire plate, so that each field of view was imaged once every 4-6 minutes over an hour. At the end, a single round of confocal imaging in the 405 and 488 channels was performed, followed by immediate fixation with PFA.

GRL-PRISM

pAAV.hSyn.iGluSnFR3.v857.GPI was a gift from Kaspar Podgorski (Addgene viral prep # 178331-AAV1). At DIV 9 and until imaging, neurons were transduced with AAV1 vectors carrying iGluSnFR3.v857.GPI[38] at 10^5 MOI. Prior to imaging, neurons were treated with 10uM Hoechst for 10min then replaced with pre-equilibrated

BrainPhys Imaging Medium[86] containing any indicated chemical treatment. Glutamate imaging was done in widefield (epifluorescence) format in bursts of 50-100 20ms exposure frames in the 488 channel and minimal power, leading to 1-2s recording windows at 50Hz. To measure spiking potentiation, the same fields of view were imaged twice, 1hr apart. After glutamate imaging, a single round of confocal imaging in the 405 and 488 channels was performed, followed by immediate fixation with PFA.

RIBOmap-PRISM

RIBOmap-PRISM primer and padlock probe sequences were generated the following way: First, 50-60nt unique hybridization regions against the coding region of the mRNA transcript of interest were identified that have minimal sequence similarity to other transcripts expressed in neurons. These regions – approximately 10-25 per target gene – were split into primer and padlock hybridization regions of 19-26nt, Tm~60C, with one nucleotide separation. Primer and padlock hybridization sequences were inserted into RIBOmap probe sequences from Zeng et al[39]. In addition, the 6-nt barcode sequences in the padlock probes were replaced with 11-nt PRISM docking sequences. The resulting full primer and padlock sequences were screened against both the rat transcriptome and against the full set of DNA-LNA probe pairs (as described above) to pick 3-5 probe pairs for each transcript of interest that have minimal crosstalk.

RIBOmap staining was performed similar to the protocol by Zeng et al. [39], with some modifications. Cultures were fixed with PFA+sucrose then permeabilized with PBS containing 0.25% Triton X-100 and 2mM Vanadyl Ribonucleoside Complex (VRC, Sigma Aldrich) for 10min at room temperature. After washing with PBS+0.1% Tween-20 (PBST), cultures were incubated with the hybridization solution overnight at 40C with shaking. Washing, ligation and amplification were performed as described by Zeng et al., except that amplification was performed for 30 minutes in most experiments and 10-160 minutes in the experiment in figure S2. Following amplification, the cultures were fixed again with 2% PFA for 10min, after which they underwent the standard PRISM protocols.

Protein-PRISM staining

Staining was performed as described previously[27,29,31,87]. Fixed cultures were permeabilized with 0.25% Triton X-100 (Sigma Aldrich) for 10min, underwent RNase treatment at 37C for 1hr, then blocked with 5%BSA (Sigma Aldrich) + 1mg/mL ssDNA (ThermoFisher) in PBS, which was also the composition for all subsequent antibody solutions. Antibody staining was performed in three steps – overnight staining with primary antibodies against targets that were imaged with secondary PRISM, then secondary staining with conjugated secondary antibodies (as well as a 488-labeled secondary antibody for the MAP2 staining), then another overnight staining round with conjugated primary antibodies. After rounds of antibody staining neurons were post-fixed with 2% PFA for 10min, then stained with 10uM Hoechst and washed with imaging buffer.

Protein- and RIBOmap-PRISM imaging

With Live-PRISM imaging, an alignment round was done imaging Hoechst and MAP2 staining simultaneously in all fields previously live imaged. Then, in every PRISM imaging round, the desired AF568- and AF647-labeled LNA imaging probes were introduced at 20nM for 10min in imaging buffer (PBS+0.5M NaCl), washed with imaging buffer and the neurons imaged in the 488, 568 and 647 channels. After each round of imaging, probes were removed by 10min incubation with 4uM invader strands in imaging buffer, followed by washes in 37C wash buffer (0.01x PBS). Before introducing the next LNA imaging probe pair, the plate was imaged again to ensure removal of the 568 and 647 signals. In experiments that imaged NR2B or Tim23 these targets were imaged in the last round with an AF568-labeled secondary antibody against Mouse IgG2b, alongside nuclear imaging with DAPI or imaging of 405-labeled probes.

Imaging setup

All imaging was done using an Opera Phenix high content spinning disk confocal microscope (PerkinElmer) at the Broad Institute CDoT. Imaging was done with a 63x water immersion objective, collecting on a 2160x2160 detector (6.5um pixel size) with 2x2 binning for 1080x1080 raw images at 0.18um/px resolution. Z-stacks of 4-7 planes (steps of 1-2um) were collected in confocal imaging. Live imaging was performed at 37C with 5% CO2.

Image processing – CAT- and Protein-PRISM and IF images

All images from calcium live, PRISM and regular immunofluorescence imaging underwent the following processing steps before alignment and analysis: 1) Calculate of an illumination profile for each channel by calculating by-pixel medians across all images of that channel, and divide the images by the illumination profile. 2) Calculate background intensities for each image consisting of the average of the 5% lowest-intensity pixels in 30x30px (for images of synapses), 60x60px (for MAP2) or 120x120px (for nuclear staining) windows and subtracting from each illumination corrected image its background image. 3) Maximum projection of images across Z-stacks.

Image processing – GRL-PRISM

Image sets from this modality underwent illumination correction and background subtraction as described above, followed by calculation of an average bleaching curve used to correct videos for photobleaching. The average of each image set was subtracted from all images of that set, and the resulting set underwent median filtering with a 5px window. The resulting filtered set was then fed into a by-pixel spike detection algorithm that labels individual pixels by the quantity and total intensity of spikes (values sufficiently higher than surrounding values) in the time plot for that pixel. All image processing was done in MATLAB with bespoke scripts (supplementary code).

Organelle segmentation and quantification

Images processed as described above were aligned across live imaging rounds, PRISM imaging rounds and between modalities, cropped, and analyzed using a bespoke CellProfiler pipeline (supplementary code) with the following core steps:

1) The DAPI image is used to identify nuclei objects. All other images of the same field are then masked by the nuclei to prevent artifacts from non-specific nuclear localization of the antibodies.
2) The MAP2 image is used to identify dendrite objects.
3) When calcium imaging was done, a maximum projection of images across the timelapse was used to extract calcium puncta. When glutamate imaging was done, the spike detection algorithm output image was used to extract glutamate spiking puncta. For all antibody-PRISM and RIBOmap-PRISM images the maximum projection image for that channel was used to extract puncta of that protein or transcript.
4) A white top hat filter with a radius of 6px is applied to all synaptic protein images across all rounds to enhance puncta.
5) For initial synapse counting analysis synaptic objects were segmented and identified in images of each channel by applying the RobustBackground tool, which calculates an optimal threshold value for each 20px window individually based on the intensity histogram. When comparing treatment groups, we used a global threshold derived from the average threshold calculated by RobustBackground across all imaged fields. We then applied this value as a uniform threshold to all images of that channel to ensure that all images are segmented identically.
6) Synapsin1 puncta are then masked using the dendrites previously identified, to retain only puncta which are within 12px of a dendrite. These are then defined as synapses.
7) Puncta in all other channels are assigned to synapses if they overlapped with Synapsin1 puncta more than 6.25% (for postsynaptic proteins) or more than 50% (for presynaptic proteins).
8) Finally, levels of each marker – protein, phosphoprotein, ribosome-bound transcript, calcium signal at each individual time point, and glutamate spike count and intensity – per synapse are calculated as the intensity integral (or mean for mitochondria) of that protein's image across its punctum. If a certain marker did not have an identified puncta associated with a synapse, its level was marked as 0.

Soma ID and cell body counting

Extrasynaptic neuronal soma regions were identified from MAP2 images as described before [31]. Images underwent a tophat filter with a 60px kernel size which mostly removed dendrite regions and retained only non-dendrite MAP2 staining. The resulting image was then masked for nuclei and synapses from DAPI and Synapsin1 staining, respectively.

Estimate of ribosome-associated transcripts per cell for RIBOmap-PRISM was done by dividing total number of counts to total number of ID'd soma. Estimate of ribosome-associated transcripts per cell for Ribo-Seq was done using the raw counts reported by Glock et al.[12] from 200ng mRNA and estimating 30pg mRNA per neuron.

CAT-PRISM analysis

DTW was performed on mean-normalized calcium traces associated with Synapsin1 puncta using the dtw package in R[46]. This generated a distance matrix of calcium trace similarity. For each pair of calcium-positive synapses, the trace similarity distance was combined with the Euclidean distance between protein and mean calcium measurements to generate a distance matrix in combined activity-multiprotein space, which was then visualized using a UMAP projection with the umap package in R.

Bayesian network analysis and controlled edge and treatment effect calculation

Prior to Bayesian network inference on synapses, data was filtered to include only excitatory synapses (negative for Gephyrin and/or vGAT, when measured, and positive for at least one excitatory synaptic protein out of PSD95, CaMKIIa, phospho-CaMKIIa, GluR2, NR2A, NR2B, vGlutT1). Prior to Bayesian network inference on mitochondria, data was filtered to include only segments positive for at least three mitochondrial proteins.

Data was discretized into 20 bins (with 0 values in a separate bin) and network derivation was done using the likelihood-score-maximizing 'tabu' algorithm6 and boot.strength functions in the R package bnlearn[88], which performed 50 repeats of network inferences from resamplings of 10% of the data. This yields both the fraction of repeats in which a certain network edge appeared and the fraction of appearances in which the edge was in a specific direction.

Given a network, we define the strength of an edge between two nodes as the average correlation of the two variables across strata where the other parents of the daughter node are held constant[89,90]. That is, the strength of an edge from A to B, where B also has edges leading to it from n other variables, for example C and D with n=2, as the correlation between A and B when controlling for C and D. To estimate that, we repeated the following algorithm to calculate average correlations between A and B across strata of equal C and D:

- Sample a point (A_0, B_0, C_0, D_0)
- Find set of all points (A, B, C, D) such that $\sqrt{(C-C_0)^2+(D-D_0)^2} < \varepsilon \cdot \sqrt{n}$ where n is the number of variables to control for (2 in this example) and ε is a predetermined tolerance level set at 0.5 (smaller tolerances did not yield significantly different measures)
- If the set contains more than 5 points, calculate Pearson's correlation coefficient $cor(A,B)$ across that set.
- Average the resulting correlation measure across $20 \cdot 2^n$ such samplings.

A similar stratification procedure was done to assess the conditional effect of a certain treatment on protein A when controlling for proteins B and C. Treated and controls groups were pooled together, a point was sampled at random and a set of all points with similar B and C was found, and the $\log_2$-fold difference between the mean levels of A in treated vs control synapses was calculated and averaged across many samplings.

Unless indicated otherwise, the Bayesian networks presented include only those edges which appeared in >80% of bootstrapped repeats, edge directionality was given when this directionality appeared in >60% of bootstrapped repeats. For Bayesian network inference in Grin2a knockout mouse neurons, inference was performed separately on DIV 6 and DIV 14 data. The edges presented are only those which appeared in the networks from both datasets with edge strengths (controlled correlations) above 0.1 in both.

RNA-seq in Grin2a knockout mice

RNA-seq was performed as described previously[91]. RNA was prepared from micro-dissected tissues using RNeasy Mini Kit (Qiagen) following the manufacturer's instructions. Briefly, tissue samples were lysed and homogenized, placed into columns, and bound to the RNeasy silica membrane. Next, contaminants were washed away, columns were treated with DNase (Qiagen) to digest residual DNA, and concentrated RNA was eluted in water. RNA concentration was measured using a NanoDrop Spectrophotometer and RNA integrity (RIN) was measured with RNA pico chips (Agilent) using a 2100 Bioanalyzer Instrument (Agilent). Purified RNA

was then stored at -80°C until library preparation for bulk RNA-seq analysis. Bulk sequencing libraries were prepared using a TruSeq Stranded mRNA Kit (Illumina) following the manufacturer's instructions. 200 ng of isolated total RNA from each sample was used and the concentration of resulting cDNA library was measured with High Sensitivity DNA chips (Agilent) using a 2100 Bioanalyzer Instrument (Agilent). A 10 nM normalized library was pooled, and sequencing was performed on a NovaSeq S2 (Illumina).

Synaptosome proteomics in Grin2a knockout mice

Protein extraction and quantification was performed as described previously[92]. Flash-frozen DLPFC gray matter (human) or whole cortex (mice) was dounce-homogenized in ice-cold homogenization buffer (5 mM HEPES pH 7.4, 1 mM MgCl2, 0.5 mM CaCl2, supplemented with phosphatase and protease inhibitors). The homogenate was centrifuged for 10 minutes at 1,400 g (4°C) and the supernatant was re-centrifuged at 13,800 g for 10 minutes (4°C). The resulting pellet was resuspended in 0.32 M Sucrose, 6mM Tris-HCl (pH 7.5) and layered gently on a 0.85 M, 1 M, 1.2 M discontinuous sucrose gradient (in 6mM Tris-HCl pH 7.5) and ultracentrifuged at 82,500 g for 2 hours (4°C). The synaptosome fraction—which sediments at the 1 M and 1.2 M sucrose interface—was collected, an equal volume of ice-cold 1% Triton X-100 (in 6mM Tris-HCl pH 7.5) was added, mixed thoroughly and incubated on ice for 15 minutes. The mixture was ultracentrifuged at 32,800 g for 20 minutes (4°C), and the final synapse protein pellet was collected by resuspension in 1% SDS. A small aliquot was taken to measure the protein concentration using the BCA assay (ThermoFisher Scientific), and the remaining protein was stored at -80°C until being processed. Protein from purified synaptic fractions was digested as described above. 100 µg of each sample was labeled with a TMT16 reagent following the protocol described above. The combined sample was fractionated on a 4.6 mm x 250 mm Zorbax 300 extend-c18 column (Agilent) and concatenated into 18 fractions for LC-MS/MS analysis.

Cross-animal prediction using Support Vector Machine learning

SVM learning was done using scikit-learn in Python (supplementary code). Synapse data obtained from CellProfiler was scaled to the 0-1 range by frequency-based discretization. The synapses from each well were randomly divided into sets of 200 synapses, each set representing a single multimodal distribution datapoint. Each datapoint consisted of either only averages of synaptic measurements of different variables across the set, or averages along with pairwise correlations between all variables. Datapoints were divided into training and testing data from different animals. Nonlinear binary classification SVMs were trained on the training data and ROC curves were generated for the test data. Hyperparameter optimization for gamma and C parameters was done using a grid search for each training run. All possible combinations of test-train data divisions were tested to generate standard deviations and errors on ROC curves.

For Grin2a knockout neuron measurements, all neurons came from eight pups from the same pregnant rat and all data was collected on the same day in the same plate. Training data (Het vs WT) consisted of all the wells from three heterozygous knockout and two wild-type pups, testing data consisted of the wells from the other two knockout and the third wild-type pup. For APV treatment measurements, training data (untreated vs treated) consisted of measurements in one experiment from one E18 rat hippocampus, and test data from a separate experiment using a different E18 hippocampus from a different pregnant rat. For RNAi measurements, each of four plates consisted of neurons from 1-3 pups of a different pregnant rat. Training data (specific gene siRNA vs nontargeting siRNA) consisted of all the wells from two plates, and test data from the other two plates.

Table 1: Labeling strategies used in this study. Listed targets were labeled either with a primary PRISM antibody a secondary PRISM antibody (docking strand labeled green), or a secondary fluorophore antibody (labeled blue).

Target	Primary Probe(s)	Secondary Probe(s)	Used in Figure(s)
MAP2	Chicken a-MAP2	Donkey anti-Chicken **AF488**	All
Synapsin1	Mouse a-Synapsin1 – **D29**		1,2,5,6,7,S5,S6
	Mouse IgG1 a-Synapsin1	Gt a-Ms IgG1 – **D9**	4,7
	Goat a-Synapsin1	Donkey a-Gt – **AF405**	3,7a,S2
vGluT1	Mouse a-vGluT1 – **D13**		1,2
Bassoon	Mouse a-Bassoon – **D8**		1,2,4,6,7,S5,S6
F-actin	Phalloidin – **D3**		1,2,4,6,7,S5,S6
CaMKIIa	Mouse IgG1 a-CaMKIIa	Gt a-Ms IgG1 – **D9**	2,6,7,S5,S6,S7
		Dk a-Ms – **AF647**	7
	Mouse a-CaMKIIa – **D2**		1,7
PSD95	Rabbit a-PSD95	Gt a-Rb – **D1**	1,2,6,7,S5,S6
		Dk a-Rb – **AF568**	3
GluR2	Guinea Pig a-GluR2	Gt a-GP – **D19**	1,2,5,6,7,S5,S6,S7
		Gt a-GP – **AF488**	S1
	Rabbit a-GluR2	Dk a-Rb – **AF568**	7a
NR1	Mouse IgG2a a-NR1	Gt a-Ms IgG2a – **D23**	1
		Gt a-Ms IgG2a – **D7**	2
NR2A	Mouse a-NR2A – **D20**		4,6,7,S5,S6,S7
NR2B	Mouse IgG2b – a-NR2B	Gt a-Ms IgG2b – **AF568**	1,2,6,7,S5,S6,S7
	Mouse a-NR2B – **D17**		7
p-CaMKIIa	Rabbit a-p-CaMKIIa (Thr286) – **D04**		2
	Rabbit a-p-CaMKIIa (Thr286)	Dk a-Rb – **AF568**	S1
Puromycin	Ms IgG2a a-Puromycin	Gt a-Ms IgG2a – **D23**	7
		Gt a-Ms IgG2a – **D7**	6,S5,S6
p-TrkB	Rabbit a-p-TrkB – **D26**		4
p-Akt	Rabbit a-p-Akt – **D4**		4
p-P70S6K	Rabbit a-p-S6K – **D25**		4
p-S6RP	Rabbit a-p-S6RP	Gt a-Rb – **D1**	4
TOMM40	Rabbit a-TOMM40 – **D2**		5,S3
TOMM20	Mouse a-TOMM20 – **D3**		5,S3
TIM23	Mouse IgG2b a-Tim23	Gt a-Ms IgG2b – **AF568**	5,S3
CoxII	Mouse IgG2a a-CoxII	Gt a-Ms IgG2a – **D23**	5,S3
CoxIV	Rabbit a-CoxIV	Gt a-Rb – **D1**	5,S3
UQCRC2	Rabbit a-UQCRC2 – **D7**		5,S3
NDUFA9	Mouse IgG1 a-NDUFA9	Gt a- Ms IgG1 – **D9**	5,S3
ATPI1F	Mouse a-ATPI1F – **D8**		5,S3

References

1 Paoletti, P., Bellone, C. & Zhou, Q. NMDA receptor subunit diversity: impact on receptor properties, synaptic plasticity and disease. *Nat Rev Neurosci* **14**, 383-400 (2013). https://doi.org/10.1038/nrn3504

2 Gao, C., Tronson, N. C. & Radulovic, J. Modulation of behavior by scaffolding proteins of the post-synaptic density. *Neurobiol Learn Mem* **105**, 3-12 (2013). https://doi.org/10.1016/j.nlm.2013.04.014

3 Vessey, J. P. & Karra, D. More than just synaptic building blocks: scaffolding proteins of the post-synaptic density regulate dendritic patterning. *J Neurochem* **102**, 324-332 (2007). https://doi.org/10.1111/j.1471-4159.2007.04662.x

4 Thomas, M. G., Pascual, M. L., Maschi, D., Luchelli, L. & Boccaccio, G. L. Synaptic control of local translation: the plot thickens with new characters. *Cell Mol Life Sci* **71**, 2219-2239 (2014). https://doi.org/10.1007/s00018-013-1506-y

5 Sutton, M. A. & Schuman, E. M. Local translational control in dendrites and its role in long-term synaptic plasticity. *J Neurobiol* **64**, 116-131 (2005). https://doi.org/10.1002/neu.20152

6 Collins, M. O. *et al.* Proteomic analysis of in vivo phosphorylated synaptic proteins. *J Biol Chem* **280**, 5972-5982 (2005). https://doi.org/10.1074/jbc.M411220200

7 Woolfrey, K. M. & Dell'Acqua, M. L. Coordination of Protein Phosphorylation and Dephosphorylation in Synaptic Plasticity. *J Biol Chem* **290**, 28604-28612 (2015). https://doi.org/10.1074/jbc.R115.657262

8 Brockhaus, J., Bruggen, B. & Missler, M. Imaging and Analysis of Presynaptic Calcium Influx in Cultured Neurons Using synGCaMP6f. *Front Synaptic Neurosci* **11**, 12 (2019). https://doi.org/10.3389/fnsyn.2019.00012

9 Bai, F. & Witzmann, F. *Synaptosome Proteomics*. 77-98 (2007).

10 Heo, S. *et al.* Identification of long-lived synaptic proteins by proteomic analysis of synaptosome protein turnover. *Proc Natl Acad Sci U S A* **115**, E3827-E3836 (2018). https://doi.org/10.1073/pnas.1720956115

11 van Oostrum, M. *et al.* The proteomic landscape of synaptic diversity across brain regions and cell types. *Cell* **186**, 5411-5427 e5423 (2023). https://doi.org/10.1016/j.cell.2023.09.028

12 Glock, C. *et al.* The translatome of neuronal cell bodies, dendrites, and axons. *Proc Natl Acad Sci U S A* **118** (2021). https://doi.org/10.1073/pnas.2113929118

13 Kawashima, T., Okuno, H. & Bito, H. A new era for functional labeling of neurons: activity-dependent promoters have come of age. *Front Neural Circuits* **8**, 37 (2014). https://doi.org/10.3389/fncir.2014.00037

14 Piehowski, P. D. *et al.* Automated mass spectrometry imaging of over 2000 proteins from tissue sections at 100-mum spatial resolution. *Nat Commun* **11**, 8 (2020). https://doi.org/10.1038/s41467-019-13858-z

15 Campagnola, L. *et al.* Local connectivity and synaptic dynamics in mouse and human neocortex. *Science* **375**, eabj5861 (2022). https://doi.org/10.1126/science.abj5861

16 Zhu, F. *et al.* Architecture of the Mouse Brain Synaptome. *Neuron* **99**, 781-799 e710 (2018). https://doi.org/10.1016/j.neuron.2018.07.007

17 Lima Caldeira, G., Peca, J. & Carvalho, A. L. New insights on synaptic dysfunction in neuropsychiatric disorders. *Curr Opin Neurobiol* **57**, 62-70 (2019). https://doi.org/10.1016/j.conb.2019.01.004

18 Penzes, P., Cahill, M. E., Jones, K. A., VanLeeuwen, J. E. & Woolfrey, K. M. Dendritic spine pathology in neuropsychiatric disorders. *Nat Neurosci* **14**, 285-293 (2011). https://doi.org/10.1038/nn.2741

19 Tomasetti, C. *et al.* Treating the Synapse in Major Psychiatric Disorders: The Role of Postsynaptic Density Network in Dopamine-Glutamate Interplay and Psychopharmacologic Drugs Molecular Actions. *Int J Mol Sci* **18** (2017). https://doi.org/10.3390/ijms18010135

20 Tononi, G. & Cirelli, C. Sleep and the price of plasticity: from synaptic and cellular homeostasis to memory consolidation and integration. *Neuron* **81**, 12-34 (2014). https://doi.org/10.1016/j.neuron.2013.12.025

21 Willsey, A. J. & State, M. W. Autism spectrum disorders: from genes to neurobiology. *Curr Opin Neurobiol* **30**, 92-99 (2015). https://doi.org/10.1016/j.conb.2014.10.015

22 Wondolowski, J. & Dickman, D. Emerging links between homeostatic synaptic plasticity and neurological disease. *Front Cell Neurosci* **7**, 223 (2013). https://doi.org/10.3389/fncel.2013.00223

23 Zimmerman, A. J. *et al.* A psychiatric disease-related circular RNA controls synaptic gene expression and cognition. *Mol Psychiatry* **25**, 2712-2727 (2020). https://doi.org/10.1038/s41380-020-0653-4

24 Zoghbi, H. Y. & Bear, M. F. Synaptic dysfunction in neurodevelopmental disorders associated with autism and intellectual disabilities. *Cold Spring Harb Perspect Biol* **4** (2012). https://doi.org/10.1101/cshperspect.a009886

25 Duman, R. S., Aghajanian, G. K., Sanacora, G. & Krystal, J. H. Synaptic plasticity and depression: new insights from stress and rapid-acting antidepressants. *Nat Med* **22**, 238-249 (2016). https://doi.org/10.1038/nm.4050

26 Duman, R. S. & Li, N. A neurotrophic hypothesis of depression: role of synaptogenesis in the actions of NMDA receptor antagonists. *Philos Trans R Soc Lond B Biol Sci* **367**, 2475-2484 (2012). https://doi.org/10.1098/rstb.2011.0357
27 Guo, S. M. *et al.* Multiplexed and high-throughput neuronal fluorescence imaging with diffusible probes. *Nat Commun* **10**, 4377 (2019). https://doi.org/10.1038/s41467-019-12372-6
28 Tomov, M. L. *et al.* Resolving cell state in iPSC-derived human neural samples with multiplexed fluorescence imaging. *Commun Biol* **4**, 786 (2021). https://doi.org/10.1038/s42003-021-02276-x
29 Danielson, E. *et al.* Molecular Diversity of Glutamatergic and GABAergic Synapses from Multiplexed Fluorescence Imaging. *eNeuro* **8** (2021). https://doi.org/10.1523/ENEURO.0286-20.2020
30 Unterauer, E. M. *et al.* Spatial proteomics in neurons at single-protein resolution. *Cell* **187**, 1785-1800 e1716 (2024). https://doi.org/10.1016/j.cell.2024.02.045
31 Falkovich, R. *et al.* A synaptic molecular dependency network in knockdown of autism- and schizophrenia-associated genes revealed by multiplexed imaging. *Cell Rep* **42**, 112430 (2023). https://doi.org/10.1016/j.celrep.2023.112430
32 Gasparini, S., Saviane, C., Voronin, L. L. & Cherubini, E. Silent synapses in the developing hippocampus: lack of functional AMPA receptors or low probability of glutamate release? *Proceedings of the National Academy of Sciences of the United States of America* **97 17**, 9741-9746 (2000).
33 Malenka, R. C. & Nicoll, R. A. Silent Synapses Speak Up. *Neuron* **19**, 473-476 (1997). https://doi.org/10.1016/S0896-6273(00)80362-1
34 Das, S., Vera, M., Gandin, V., Singer, R. H. & Tutucci, E. Intracellular mRNA transport and localized translation. *Nature Reviews Molecular Cell Biology* **22**, 483-504 (2021). https://doi.org/10.1038/s41580-021-00356-8
35 Darnell, J. C. *et al.* FMRP stalls ribosomal translocation on mRNAs linked to synaptic function and autism. *Cell* **146**, 247-261 (2011). https://doi.org/10.1016/j.cell.2011.06.013
36 Ifrim, M. F., Williams, K. R. & Bassell, G. J. Single-Molecule Imaging of PSD-95 mRNA Translation in Dendrites and Its Dysregulation in a Mouse Model of Fragile X Syndrome. *J Neurosci* **35**, 7116-7130 (2015). https://doi.org/10.1523/JNEUROSCI.2802-14.2015
37 Meacham, J. The Eight Best Green Fluorescent Calcium Indicators.
38 Aggarwal, A. *et al.* Glutamate indicators with improved activation kinetics and localization for imaging synaptic transmission. *Nat Methods* **20**, 925-934 (2023). https://doi.org/10.1038/s41592-023-01863-6
39 Zeng, H. *et al.* Spatially resolved single-cell translatomics at molecular resolution. *Science* **380**, eadd3067 (2023). https://doi.org/10.1126/science.add3067
40 Cervantes, J., Garcia-Lamont, F., Rodríguez-Mazahua, L. & Lopez, A. A comprehensive survey on support vector machine classification: Applications, challenges and trends. *Neurocomputing* **408**, 189-215 (2020). https://doi.org/10.1016/j.neucom.2019.10.118
41 Higley, M. J. & Sabatini, B. L. Calcium signaling in dendrites and spines: practical and functional considerations. *Neuron* **59**, 902-913 (2008). https://doi.org/10.1016/j.neuron.2008.08.020
42 Siegel, F. & Lohmann, C. Probing synaptic function in dendrites with calcium imaging. *Exp Neurol* **242**, 27-32 (2013). https://doi.org/10.1016/j.expneurol.2012.02.007
43 VOLFOVSKY, N., PARNAS, H., SEGAL, M. & KORKOTIAN, E. Geometry of Dendritic Spines Affects Calcium Dynamics in Hippocampal Neurons: Theory and Experiments. *The American Physiological Society* (1999).
44 Yuste, R., Majewska, A., Cash, S. S. & Denk, W. Mechanisms of Calcium Influx into Hippocampal Spines: Heterogeneity among Spines, Coincidence Detection by NMDA Receptors, and Optical Quantal Analysis. *The Journal of Neuroscience* **19** (1999).
45 Yuste, R., Majewska, A. & Holthoff, K. From form to function: calcium compartmentalization in dendritic spines. *Nature Neuroscience* **3** (2000).
46 Giorgino, T. Computing and Visualizing Dynamic Time Warping Alignments in R: The dtw Package. *Journal of Statistical Software* **31**, 1-24 (2009).
47 Cane, M., Maco, B., Knott, G. & Holtmaat, A. The relationship between PSD-95 clustering and spine stability in vivo. *J Neurosci* **34**, 2075-2086 (2014). https://doi.org/10.1523/JNEUROSCI.3353-13.2014
48 Oosawa, F. Size distribution of protein polymers. *Journal of Theoretical Biology* (1970).
49 Sun, C. *et al.* The prevalence and specificity of local protein synthesis during neuronal synaptic plasticity. *Science Advances* **7** (2021).
50 Minichiello, L. *et al.* Mechanism of TrkB-Mediated Hippocampal Long-Term Potentiation. *Neuron* **36**, 121-137 (2002).

51 Yoshii, A. & Constantine-Paton, M. Postsynaptic BDNF-TrkB signaling in synapse maturation, plasticity, and disease. *Dev Neurobiol* **70**, 304-322 (2010). https://doi.org/10.1002/dneu.20765
52 Yoshii, A. & Constantine-Paton, M. BDNF induces transport of PSD-95 to dendrites through PI3K-AKT signaling after NMDA receptor activation. *Nat Neurosci* **10**, 702-711 (2007). https://doi.org/10.1038/nn1903
53 Magnuson, B., Ekim, B. & Fingar, Diane C. Regulation and function of ribosomal protein S6 kinase (S6K) within mTOR signalling networks. *Biochemical Journal* **441**, 1-21 (2011). https://doi.org/10.1042/bj20110892
54 Pfanner, N., Warscheid, B. & Wiedemann, N. Mitochondrial proteins: from biogenesis to functional networks. *Nat Rev Mol Cell Biol* **20**, 267-284 (2019). https://doi.org/10.1038/s41580-018-0092-0
55 Varabyova, A., Stojanovski, D. & Chacinska, A. Mitochondrial protein homeostasis. *IUBMB Life* **65**, 191-201 (2013). https://doi.org/10.1002/iub.1122
56 Yang, J. S. *et al.* Spatial and functional organization of mitochondrial protein network. *Sci Rep* **3**, 1403 (2013). https://doi.org/10.1038/srep01403
57 Rackham, O. & Filipovska, A. Organization and expression of the mammalian mitochondrial genome. *Nat Rev Genet* **23**, 606-623 (2022). https://doi.org/10.1038/s41576-022-00480-x
58 Rehling, P., Brandner, K. & Pfanner, N. Mitochondrial import and the twin-pore translocase. *Nat Rev Mol Cell Biol* **5**, 519-530 (2004). https://doi.org/10.1038/nrm1426
59 Bahat, A. & Gross, A. Mitochondrial plasticity in cell fate regulation. *J Biol Chem* **294**, 13852-13863 (2019). https://doi.org/10.1074/jbc.REV118.000828
60 Mattson, M. P., Gleichmann, M. & Cheng, A. Mitochondria in neuroplasticity and neurological disorders. *Neuron* **60**, 748-766 (2008). https://doi.org/10.1016/j.neuron.2008.10.010
61 Li, J. *et al.* Association of Mitochondrial Biogenesis With Variable Penetrance of Schizophrenia. *JAMA Psychiatry* **78**, 911-921 (2021). https://doi.org/10.1001/jamapsychiatry.2021.0762
62 Vos, M., Lauwers, E. & Verstreken, P. Synaptic mitochondria in synaptic transmission and organization of vesicle pools in health and disease. *Frontiers in synaptic neuroscience* **2**, 139 (2010).
63 Sirrenberg, C. *et al.* Functional cooperation and stoichiometry of protein translocases of the outer and inner membranes of mitochondria. *J Biol Chem* **272**, 29963-29966 (1997). https://doi.org/10.1074/jbc.272.47.29963
64 Righi, M., Tongiorgi, E. & Cattaneo, A. Brain-Derived Neurotrophic Factor (BDNF) Induces Dendritic Targeting of BDNF and Tyrosine Kinase B mRNAs in Hippocampal Neurons through a Phosphatidylinositol-3 Kinase-Dependent Pathway. *The Journal of Neuroscience* **20**, 3165-3174 (2000). https://doi.org/10.1523/jneurosci.20-09-03165.2000
65 Volkmann, R. A. *et al.* MPX-004 and MPX-007: New Pharmacological Tools to Study the Physiology of NMDA Receptors Containing the GluN2A Subunit. *PLoS One* **11**, e0148129 (2016). https://doi.org/10.1371/journal.pone.0148129
66 Lisman, J., Yasuda, R. & Raghavachari, S. Mechanisms of CaMKII action in long-term potentiation. *Nat Rev Neurosci* **13**, 169-182 (2012). https://doi.org/10.1038/nrn3192
67 Singh, T. *et al.* Rare coding variants in ten genes confer substantial risk for schizophrenia. *Nature* **604**, 509-516 (2022). https://doi.org/10.1038/s41586-022-04556-w
68 Herzog, L. E. *et al.* Mouse mutants in schizophrenia risk genes GRIN2A and AKAP11 show EEG abnormalities in common with schizophrenia patients. *Translational Psychiatry* **13**, 92 (2023). https://doi.org/10.1038/s41398-023-02393-7
69 Dreosti, E., Odermatt, B., Dorostkar, M. M. & Lagnado, L. A genetically encoded reporter of synaptic activity in vivo. *Nat Methods* **6**, 883-889 (2009). https://doi.org/10.1038/nmeth.1399
70 Oh, J., Lee, C. & Kaang, B. K. Imaging and analysis of genetically encoded calcium indicators linking neural circuits and behaviors. *Korean J Physiol Pharmacol* **23**, 237-249 (2019). https://doi.org/10.4196/kjpp.2019.23.4.237
71 Zhang, Y. *et al.* Fast and sensitive GCaMP calcium indicators for imaging neural populations. *Nature* **615**, 884-891 (2023). https://doi.org/10.1038/s41586-023-05828-9
72 Yang, S. J., Del Bonis-O'Donnell, J. T., Beyene, A. G. & Landry, M. P. Near-infrared catecholamine nanosensors for high spatiotemporal dopamine imaging. *Nat Protoc* **16**, 3026-3048 (2021). https://doi.org/10.1038/s41596-021-00530-4
73 Perez-Alvarez, A. *et al.* Freeze-frame imaging of synaptic activity using SynTagMA. *Nat Commun* **11**, 2464 (2020). https://doi.org/10.1038/s41467-020-16315-4

74 McKenzie, M., Lim, S. C. & Duchen, M. R. Simultaneous Measurement of Mitochondrial Calcium and Mitochondrial Membrane Potential in Live Cells by Fluorescent Microscopy. *J Vis Exp* (2017). https://doi.org/10.3791/55166
75 Abad, M. F., Di Benedetto, G., Magalhaes, P. J., Filippin, L. & Pozzan, T. Mitochondrial pH monitored by a new engineered green fluorescent protein mutant. *J Biol Chem* **279**, 11521-11529 (2004). https://doi.org/10.1074/jbc.M306766200
76 Hanson, G. T. *et al.* Investigating mitochondrial redox potential with redox-sensitive green fluorescent protein indicators. *J Biol Chem* **279**, 13044-13053 (2004). https://doi.org/10.1074/jbc.M312846200
77 Wang, W. *et al.* Superoxide flashes in single mitochondria. *Cell* **134**, 279-290 (2008). https://doi.org/10.1016/j.cell.2008.06.017
78 Wang, X. *et al.* Three-dimensional intact-tissue sequencing of single-cell transcriptional states. *Science* **361** (2018). https://doi.org/10.1126/science.aat5691
79 Soderberg, O. *et al.* Direct observation of individual endogenous protein complexes in situ by proximity ligation. *Nat Methods* **3**, 995-1000 (2006). https://doi.org/10.1038/nmeth947
80 Zhang, W., Xie, M., Shu, M. D., Steitz, J. A. & DiMaio, D. A proximity-dependent assay for specific RNA-protein interactions in intact cells. *Rna* **22**, 1785-1792 (2016). https://doi.org/10.1261/rna.058248.116
81 Chin, A. & Lecuyer, E. Puromycin Labeling Coupled with Proximity Ligation Assays to Define Sites of mRNA Translation in Drosophila Embryos and Human Cells. *Methods Mol Biol* **2381**, 267-284 (2021). https://doi.org/10.1007/978-1-0716-1740-3_15
82 Chen, X. *et al.* ATAC-see reveals the accessible genome by transposase-mediated imaging and sequencing. *Nature Methods* **13**, 1013-1020 (2016). https://doi.org/10.1038/nmeth.4031
83 Isaac, R. S. *et al.* Single-nucleoid architecture reveals heterogeneous packaging of mitochondrial DNA. *Nature Structural & Molecular Biology* **31**, 568-577 (2024). https://doi.org/10.1038/s41594-024-01225-6
84 Graber, T. E. *et al.* Reactivation of stalled polyribosomes in synaptic plasticity. *Proc Natl Acad Sci U S A* **110**, 16205-16210 (2013). https://doi.org/10.1073/pnas.1307747110
85 Ostroff, L. E. *et al.* Shifting patterns of polyribosome accumulation at synapses over the course of hippocampal long-term potentiation. *Hippocampus* **28**, 416-430 (2018). https://doi.org/10.1002/hipo.22841
86 Zabolocki, M. *et al.* BrainPhys neuronal medium optimized for imaging and optogenetics in vitro. *Nat Commun* **11**, 5550 (2020). https://doi.org/10.1038/s41467-020-19275-x
87 Veneziano, R. *et al.* Multiplexed Imaging of Neuronal Synapses Using Nucleic Acid Probe Exchange. *Protocol Exchange* (2018). https://doi.org/10.1038/protex.2018.066
88 Scutari, M. Scutari Learning Bayesian Networks with the bnlearn R Package. *Journal of Statistical Software* **35** (2010).
89 Uphoff, E. Measuring Connection Strengths and Link Strengths in Discrete Bayesian Networks. (Georgia Institute of Technology, 2007).
90 Pe'er, D. Bayesian Network Analysis of Signaling Networks - A Primer. *STKE Protocol* (2005).
91 Farsi, Z. *et al.* Brain-region-specific changes in neurons and glia and dysregulation of dopamine signaling in Grin2a mutant mice. *Neuron* **111**, 3378-3396.e3379 (2023). https://doi.org/https://doi.org/10.1016/j.neuron.2023.08.004
92 Aryal, S. *et al.* Deep proteomics identifies shared molecular pathway alterations in synapses of patients with schizophrenia and bipolar disorder and mouse model. *Cell Reports* **42** (2023). https://doi.org/10.1016/j.celrep.2023.112497